國立臺灣大學電機資訊學院光電工程學研究所

碩士論文

Graduate Institute of Photonics and Optoeletronics

College of Electrical Engineering and Computer Science

National Taiwan University

Master Thesis

利用矽核光纖製作蕭特基光偵測器

Fabrication of Schottky Photodetector by using Si-cored fibers

黃彥博

Yan-Bo Huang

指導教授：王倫 博士

Advisor: Lon A. Wang, Ph.D.

中華民國 104 年 1 月

January, 2015

國立臺灣大學碩士學位論文
口試委員會審定書

利用矽核光纖製作蕭特基光偵測器
Fabrication of Schottky Photodetector by Using Si-Cored Fibers

本論文係黃彥博君（學號 R01941079）在國立臺灣大學光電工程學研究所完成之碩士學位論文，於民國 104 年 2 月 2 日承下列考試委員審查通過及口試及格，特此證明

口試委員：

王倫（指導教授）

孟心飛　　劉致為

冉曉雯　　黃升龍

所　長　林恭如

誌謝

能完成這篇論文，首先要特別感謝是指導教授王倫老師的指導，雖然碩班一路上並不算順遂，但老師總是盡力幫我尋找與商借資源，並在實驗上給予建議與指導，特別是在其他領域實驗室聯絡方面，使我了解人際關係與溝通的重要。

在碩班期間，我要特別感謝奕鈞學長，在我碩一的時候不厭其煩的教導我各項儀器的原理和使用方法，使我之後的研究能夠應用各種機台來達到實驗目的;另外也要特別感謝方向、哲安不論是實驗上或是一些處理事情的態度及方法都讓我學習到許多，最後更不能忘了世昌、昇宏兩位學弟，陪伴我一起做實驗，解決問題，最後幫我分擔事物，使我的畢業題目可以順利完成。另外我也很感謝各個學弟在行政上的幫忙，以及一起打球、聊天，舒緩緊張的心情。也特別感謝在碩班接觸過的所有人，給予我不同的幫助與成長。

最後我要感謝我的父母家人、朋友在精神上給予支持及鼓勵，使我無後顧之憂去面對及解決各種問題。

中文摘要

近年來結合半導體材料和傳統光纖的研究主題正在迅速發展，透過這樣的結合能夠產生各式各樣的應用在矽光子領域、生醫感測領域、或是達成全光調變的可能性。

在這個論文中，我們示範了矽核光纖的製作方法，透過結合了垂直抽絲法及粉末法的特點，不需要使用昂貴的單晶矽晶棒，而改以低成本的多晶矽粉末作為代替，在經由優化製程的參數製作做出數公尺長的矽核光纖。由於矽的光學特性及電性都深深地被結晶性影響所以先針對了結晶性的部份做量測，經由穿透式電子顯微鏡及柆曼光譜儀的檢測結果證實為單晶矽之後並量測矽核光纖的光學及電的特性。

由於矽核光纖在光學特性及電性上有良好的表現，我們利用矽核光纖製作了蕭特基光偵測器，透過內部光激發的效應（internal photoemission process）使得此光偵測器能夠偵測到矽原本是在此通訊波段不吸收此波段的光。此外更由於矽核光纖天生的波導特性，能夠透過與接收端的光纖熔接，免去原本難處理的光耦合步驟。

關鍵字：半導體光纖、矽核光纖、蕭特基光偵檢器

ABSTRACT

Recently the combination of semiconductor materials with fiber optics has become one of the emerging research topics. Such combination of semiconductor and fiber optics may lead to various applications in Si photonics, bio-chemical sensing, and all-optical modulation.

In this thesis, we demonstrated a method of fabricating silicon cored fiber. In this study, a technique featuring powder-in-tube and vertical-drawing was adopted for making single-crystal Si-cored fibers. Much cheaper polycrystalline Si powders substituting expensive single-crystal Si powders or seed rods were packed into a fused silica tube. By optimizing the drawing parameters, meter-long Si-cored fibers were obtained. Because the electrical and optical characteristics of Si are much affected by the crystallinity of Si, we need first analyze the crystallinity of Si-cored fibers, and then measure their electrical and optical characteristics. The measured result showed that our Si-cored fibers displayed excellent single crystallinity confirmed by micro-Raman spectra and high-resolution transmission electron microscope images. The Si-cored fibers also exhibited outstanding optical and electrical properties.

With the above merits, a Si Schottky photodetector (SSPD) made by using a Si-cored fiber is demonstrated. Based on the internal photoemission process, SSPD can work in telecom regimes where Si is well known as transparent. Furthermore, another major advantage is that the inherent waveguide property of Si-cored fiber enabled an SSPD to be spliced with a receiving silica fiber, which can eliminate the need of cumbersome optical coupling.

Keywords: semiconductor fibers、silicon cored fibers、Schottky photodetector

Statement of Contributions

Original Contributions

1. Fabrication of Schottky photodetector by using Si-cored fibers.

General Contributions

1. Cooperating with Jian-Hong Chen to splice Si-cored fiber and Si microfiber by using arc discharge device.

2. Cooperating with Yi-Chuan Tseng and Che-An Lin to measure characteristics of Si-cored fibers.

3. Cooperating with Yi-Chuan Tseng, Che-An Lin, Sheng-Hung Chen, Shih-Chang Syu to optimize the drawing parameters of Si-cored fiber. (Cracks in the interface between silica cladding and silicon core were reduced substantially ; The outer diameter of Si-cored fibers was decreased to 100 μm.)

CONTENTS

LIST OF FIGURES

LIST OF TABLES

Chapter 1 Introduction

1.1 Motivation

Semiconductor waveguide fabrication for photonics applications is usually fabricated in a planar geometry. However, over the past decade a new field of semiconductor-based optical fiber devices which combined semiconductor materials with fiber optics has emerged. Compared to the conventional optical fibers made from silica, the glass-clad and semiconductor cored optical fibers provide ideal hosts for the manipulation of both photons and electrons due to their mid infrared transparency, high optical nonlinearities and semiconductor properties [1-4]. In addition, this kind of combination offers a number of unique advantages in that, not only is the active semiconductor functionality now embedded seamlessly within the transmission medium, but these semiconductor fibers are robust, flexible, and can be fabricated to have long electromagnetic interaction lengths. In contrast to planar rib and ridge waveguides with rectilinear cross sections that generally give rise to polarization dependence, the cylindrical fiber waveguides have the advantage of a circular, polarization-independent cross section. Such combination of semiconductor and fiber optics may lead to various applications in silicon photonics, bio-chemical sensing, and all-optical modulation [5-7]. Over the past decade several materials prepared for semiconductor-based optical fiber devices have been investigated, including Zinc Selenide (ZnSe), germanium (Ge) and silicon (Si) [8-9]. Among many properties, transmission loss and crystallinity are the two major figures of merit for the efficacies of their optical and electronic applications, respectively. ZnSe fibers capable of hosting transition metal ions showed low transmission loss of ca. 0.5-0.9 dB/cm in the wavelengths ranging from 500 nm to 22 μm [8]. Ge fibers were reported with optical transmission loss of ca. 20 dB/cm in the wavelengths from 2 to 11 μm. Transmission losses of the Si-cored fibers are found strongly correlated to the crystallinity of the Si-core, which in turn is determined by such parameters as fabrication methods, source materials, etc.

In this work, a combined techniques of powder-in-tube and vertical-drawing were adopted for making single-crystal Si-cored fibers. Much cheaper polycrystalline Si powders substituting expensive single-crystal Si seed rods were packed into a fused silica tube. By optimizing the drawing parameters, meter-long Si-cored fibers were obtained with ultralow transmission losses because the entire lengths of Si cores were single crystalline.

A way of detecting infrared sub-bandgap optical radiation in silicon is to apply the internal photoemission process using a Schottky barrier PD. Schottky PDs are very attractive because of their simple material structures and fabrication process. However, the silicon waveguide based detectors generally require more complicated semiconductor fabrication process to define the waveguide region. In this thesis we fabricated Schottky PDs built directly on a silicon fiber, which can eliminate the need of complicated fabrication process because of its inherent waveguiding in the silicon cored fiber. Besides, the resultant single-crystal Si core made the fiber possess excellent optical and electrical properties which is beneficial for the performance for silicon Schottky photodetectors (SSPD). For device characterization, first, the current-voltage (I-V) characteristics of the SSPD were measured for different optical input power without any modulation. After obtaining the I-V characteristics, we measured the frequency responses of SSPDs. The amount of information which is used to convert optical to electrical signals is limited by the bandwidth of PD, therefore we would discuss about how to improve the measured frequency responses.

1.2 Organization of the Thesis

In this thesis, the fabrication of Si-cored fibers is described in details, and Schottky photodetector is made directly on Si-cored fibers. Chapter 1 decribes the motivation of this thesis. In Chapter 2, we review on fabrication method reported by other groups worldwide and then introduce our experiment setup and fabrication method. After the fabrication method, we compare the experiment results obtained at different drawing speeds in order to optimize the fabrication process. Chpater 3 describes the measured characteristics of Si-cored fibers including material, optical, electrical properties. In Chapter 4, first of all we describe the motivation of fabrication of SSPD and then introduce the theory of Schottky diode. After a brief introduction on the SSPD, the fabrication process and characteristics of SSPD including responsivity and frequency responses are described. Chapter 5 concludes this thesis and proposes future works.

Chapter 2 Fabrication of Si-cored fibers

2.1 Literature Review

Si cored fiber has been studied since its first reported in 2006 Science [1] and it can still be regarded as a new topic. The research of Si-cored fibers mainly focused on the fabrication methods, crystallinity and transmission loss, etc. Several groups has started the research and more and more researchers were involved in recent years. Here are the significant fabrication methods reported by these research groups.

2.1.1 High-pressure chemical vapor deposition method

A high-pressure chemical vapor deposition (HPCVD) method have been reported by Sazio, *et al.* since 2006 in Science [1]. High pressure mixture of precursor gas, typically of 2 MPa of SiH_4 in 38 MPa of argon contained in a stainless steel reservoir, was configured to flow through microstructured optical fibers capillaries ranging from < 50 nm to 10 μm in diameter. The schematic diagram of HPCVD for Si-cored fibers is shown in Fig. 2-1. High pressure mixtures of precursors such as SiH_4 are very toxic, so it is critical that they are handled with appropriate care. Silicon was deposited on the inner walls by heating the precursor mixture to 700℃ at a rate of 2℃/min over a length of 70 cm. The polymer cladding of the fibers was either stripped before heating or burned off during heating. Evolution of gas was monitored by placing the ends of the fibers in a hydrocarbon liquid and examining the rate of bubble formation. Since the vacuum process was involved, the fabrication of the Si-cored optical fibers might be time consuming and not cost-effective; in addition, the resultant Si-cored fibers were amorphous and had propagation loss ca. 1.7 dB/cm. Fig. 2-2 shows the optical and SEM image of silicon core fiber. A unique feature of this method is that different materials could be deposited from the outer edge to the center inside the pore.

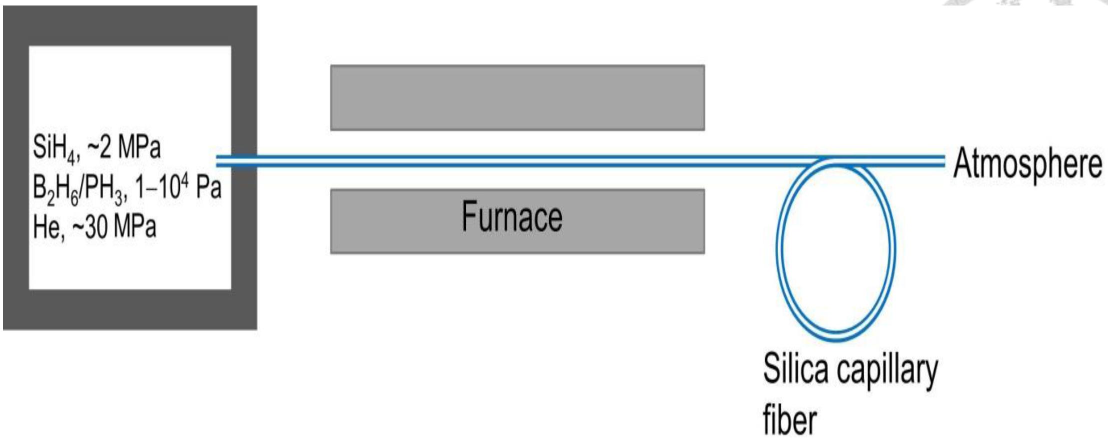

Fig. 2-1 A schematic illustration shows the high pressure chemical vapor deposition for Si-cored fibers. [1]

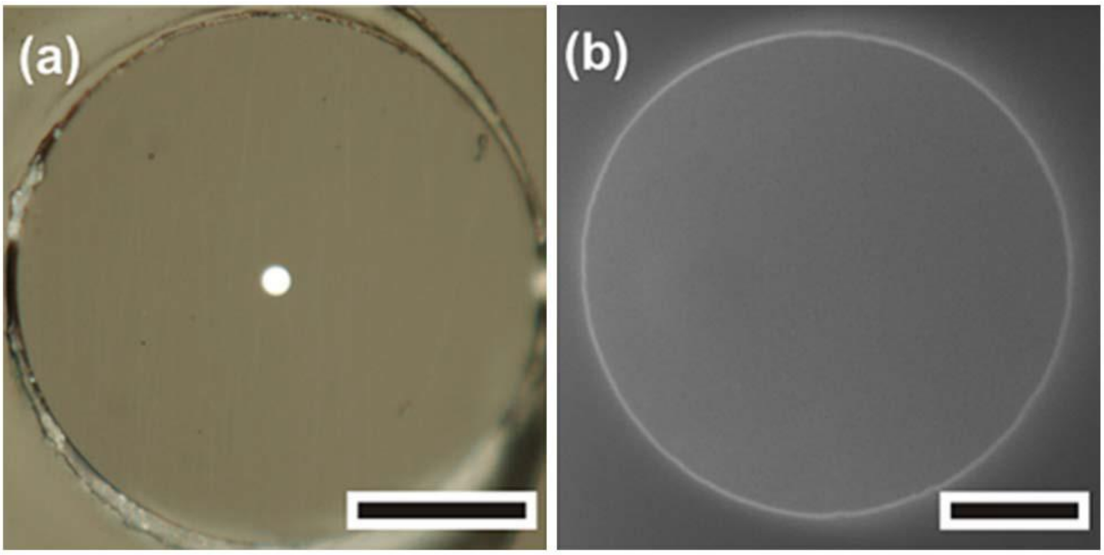

Fig. 2-2 (a) Optical microscope image of the 5.6 µm polysilicon core fiber, scale bar 50 µm. (b) SEM image of the 1.3 µm core, scale bar 400 nm. [1]

2.1.2 Molten core method.

In the light of CZ and FZ methods, J. Ballato’s and S. Morris’s groups proposed the molten core drawing method with an attempt to make a single-crystal Si-cored fiber. Three tubes of optical quality silica were sleeved concentrically to yield an overall cladding with outer diameter about 50 mm and inner diameter of 3.5 mm. A section of bulk silica rod was joined to one end of this tube assembly to act as a seal for the silicon core, which would be molten during the draw. This approach to layering of concentric tubes was utilized since a single glass tube of those dimensions was not commercially available. Such a thick-walled cladding tube was chosen to mitigate potential issue with the weight of the molten silicon leaking out or otherwise deforming the softened cladding glass during the draw. A rod of silicon measured about 3 mm in diameter by about 40 mm in length, which had been core drilled out of a Czochralski-grown single crystal boule, was sleeved into this end-sealed silica tube assembly. Fibers were drawn at Clemson University using the Heathway draw tower at temperatures conventionally used for fabricating telecommunication-grade silica fibers (approximately 1950℃). At these temperatures, the silicon core is well above its melting point and the melt is then encapsulated by the viscous silica cladding. The fabrication of fibers involving the melting of the core material during the draw process was originally developed over a decade ago [2]. The fibers were thick enough to be characterized as ‘cane’ and were drawn at a rate of 2.7 m/min using a cane tracker on the draw tower. Several sizes of cane were fabricated for comparison; generally in the range of 1 to 2 mm in diameter yielding core diameters of between approximately 60 and 120 μm, respectively. Fig. 2-3 shows an SEM of the silicon core region. These diameters, which yielded lengths that were strong but not overly flexible, were simply chosen to be large enough to visually see if the core remained black during the draw process. Approximately 30 m of fiber was drawn, though, due to its relatively thick diameter, fibers were scribed off in approximately 1.5 m lengths.

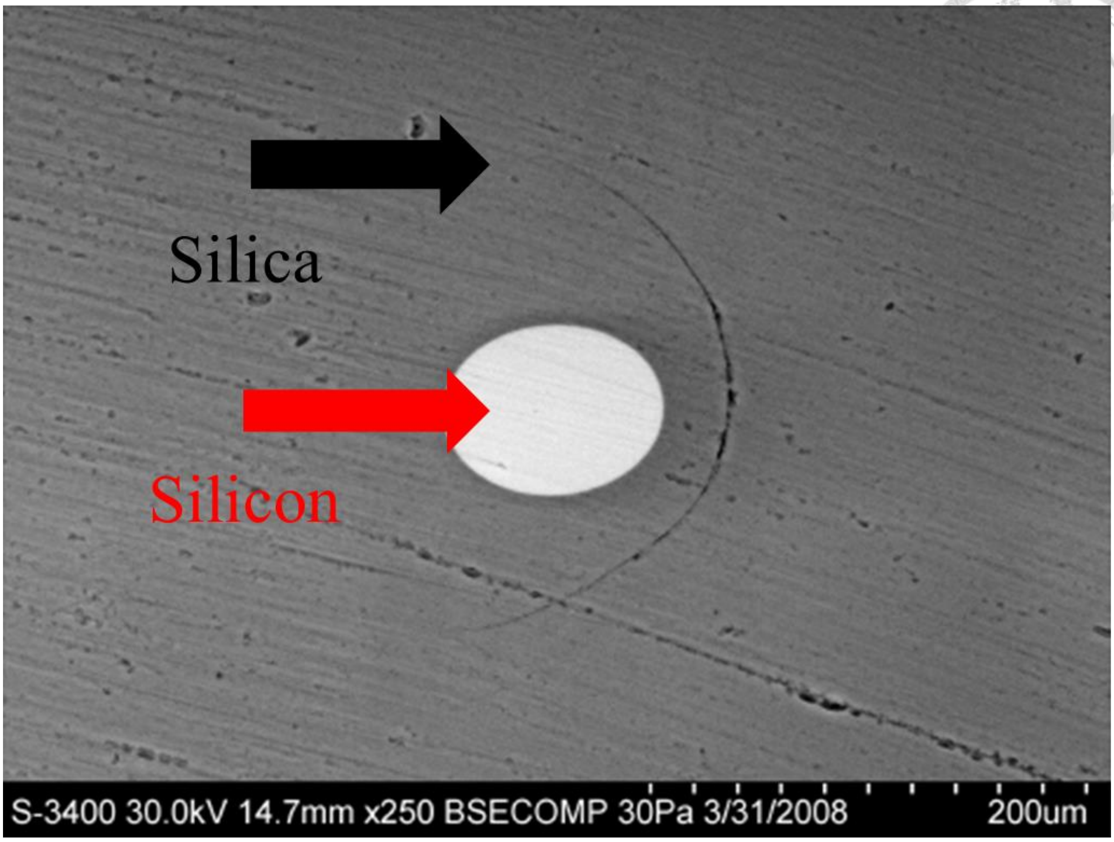

Fig. 2-3 SEM of the core region of the silicon core, silica-clad optical fiber. [3]

2.1.3 Powder in tube method

Recently, the use of powders to substitute single-crystal rods in the horizontal drawing system has been demonstrated by S. Morris et al. In their work, silicon optical fibers were made with the powder-in-tube technique. The preform was made in such a way that high-purity silicon powders were placed inside the optical-purity silica tube, with an outer diameter of 6 mm and an inner diameter of 3 mm. Silicon optical fibers were fabricated from the preform by utilizing a custom-made fiber drawing system, as illustrated in Fig. 2-4. This system was specifically designed for specialty fiber drawing. The fiber drawing system had two chucks, which were used to clamp the silica preform and could spin together or separately at precisely controlled speeds. The second chuck could also be moved linearly, which drew the fiber from the preform when heated and softened by a hydrogen-oxygen torch over 1600 ℃.

The preform was clamped in one of the chucks, and another silica tube was clamped in the second chuck, which served to support and allowed mechanical force to be imparted on the molten preform. The preform was set to spin by slowly rotating the two chucks at the same rate in order to be heated uniformly. When the preform was heated by the hydrogen-oxygen flame to a temperature over 1600℃, the silicon was melted and the silica tube was softened. Silicon optical fiber was produced by moving the second chuck along the platform, which maintains linearity. A vacuum was applied during the fabrication process in order to remove air from the preform. The vacuum was maintained as the preform was heated and during the fiber drawing. The fiber drawing system has the ability to control parameters such as the fiber diameter and the length, fiber drawing speed, etc. The fabricated silicon optical fibers have cladding diameters in the range of 40 to 240 μm and core diameters in the range of 10 to 100 μm and an approximate overall length of 7 cm, as shown in Fig. 2-5 and Fig. 2-6.

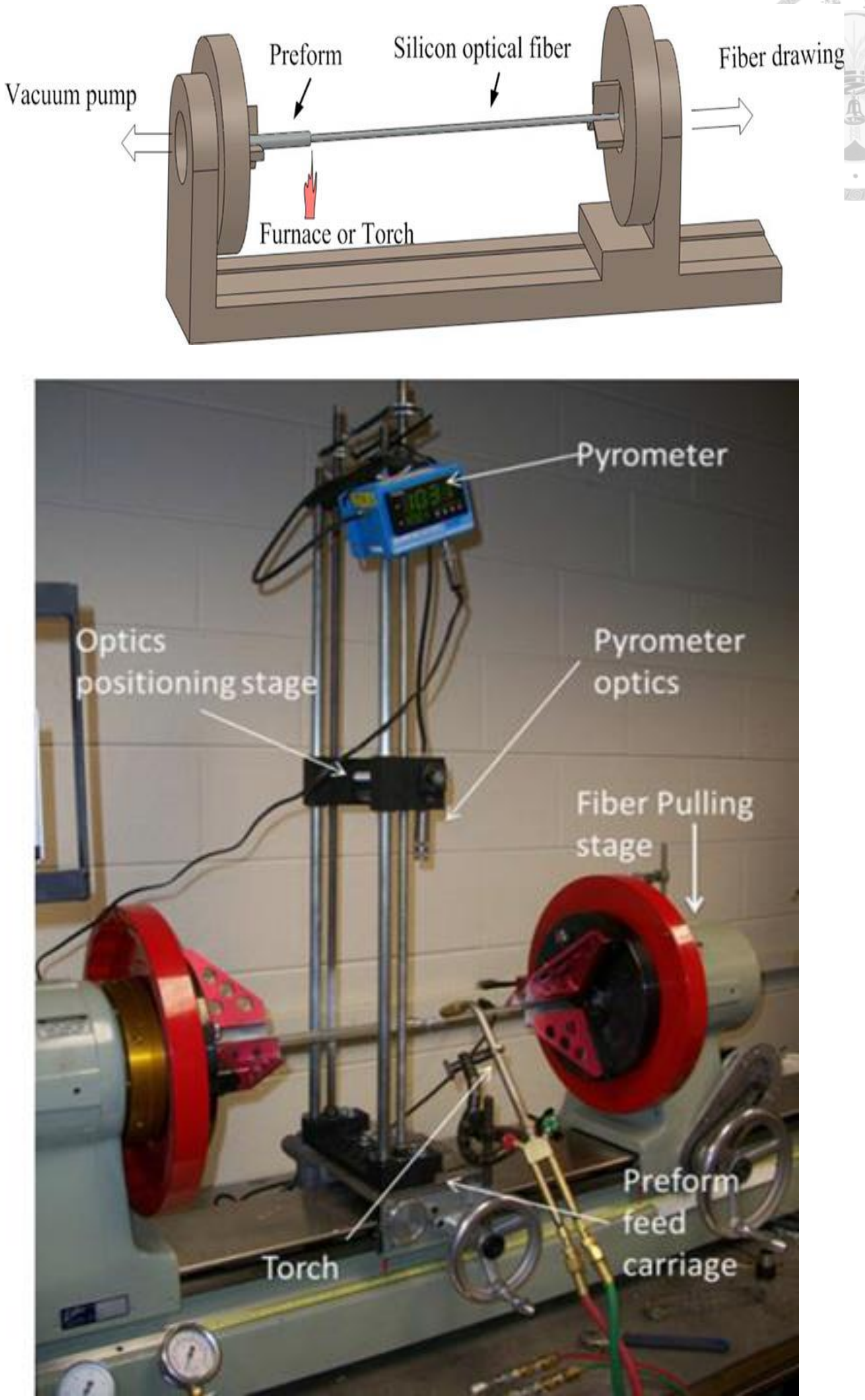

Fig. 2-4 Illustration of the silicon optical fiber drawing system. [4]

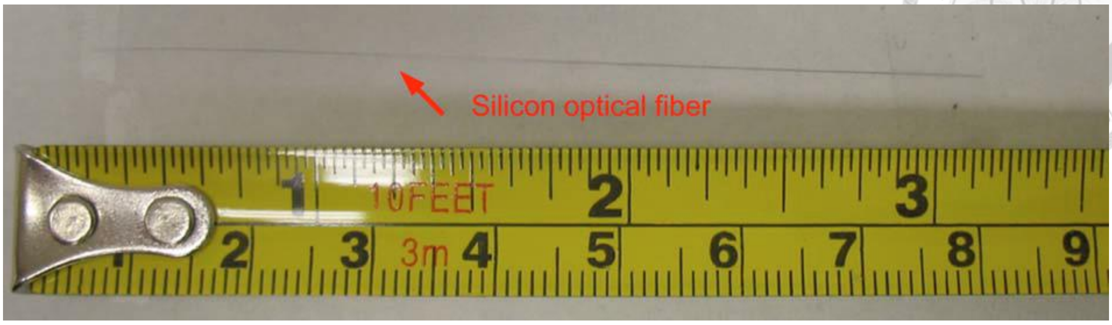

Fig. 2-5 An approximately 7-cm-long silicon optical fiber. [4]

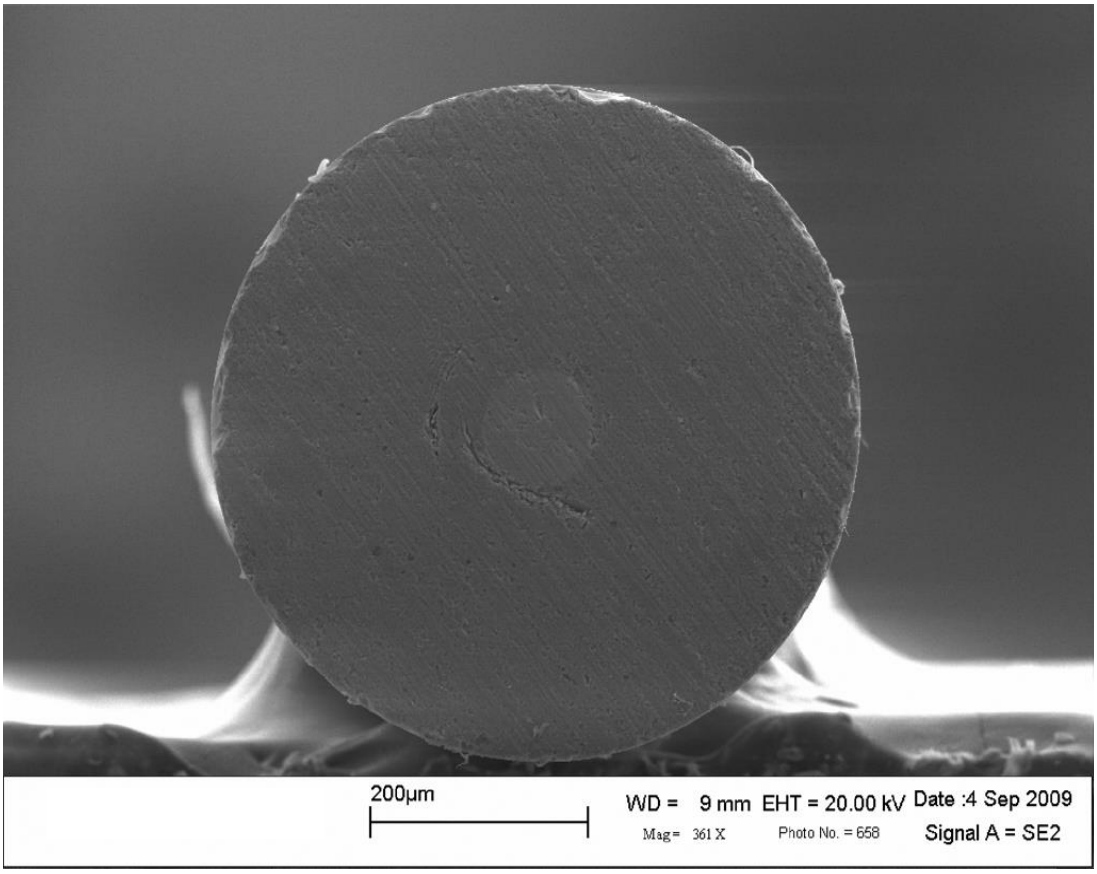

Fig. 2-6.An SEM micrograph of silicon optical fiber. [4]

2.2 A Si-cored Fiber Drawing Tower

The Si-cored fiber drawing tower is the equipment which is modified from the conventional optical fiber drawing tower [5-7]. The whole system includes a furnace, a feeding mechanism, a cooling system, a vacuum pump, and a heating control panel. Fig. 2-7 shows the experimental setup of Si-cored fiber drawing tower. There are some components in the furnace including a thermocouple which could detect the temperature of the furnace to let us know how to control output current appropriately, a cooling system which could control the temperature of electrodes to avoid metal electrodes from being overheated, a heating resistor which could provide enough heat to soften silica and melt silicon. A heating resistor consisted of two manufactured graphite tubes is shown in Fig. 2-8. Fig. 2-9 shows the feeding system to be used to control the holder to travel slowly to provide more materials for fiber drawing. A cooling system consisted of a water tower and waterway of furnace. Fig. 2-10 shows the cool system, which used water to cool the heat generated from the electrodes and to recycle water. Because there would be some gas which be produced during the drawing process, the vacuum pump would be employed. If there is some gas not been removed, it would block the melting silicon, resulting in discontinuous silicon blocks in Si-cored fibers. Fig. 2-11 shows the heating control panel, which controls output current to the heating resistor, providing enough heat needed to draw fibers after electric energy to heat conversion through the resistors.

(a)

(b)

Fig. 2-7 The experimental setup of Si-cored fibers drawing tower (a) side view (b) front view.

c

Fig. 2-8 Manufactured graphites tube served as a heating source.

(a) (b)

Fig. 2-9 The feeding system used to control the holder to slowly travel to provide more materials for fiber drawing: (a) control panel, (b) a silica tube holder.

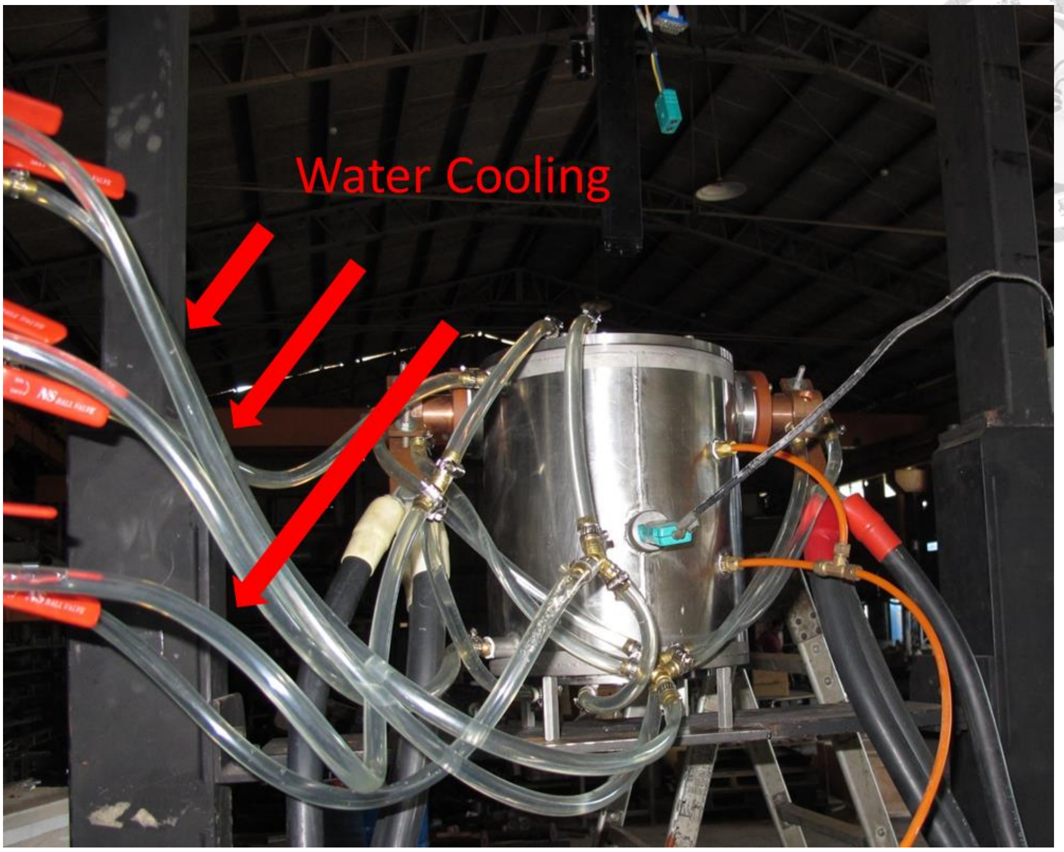

Fig. 2-10 A water cooling system used to cool the heat of electrodes.

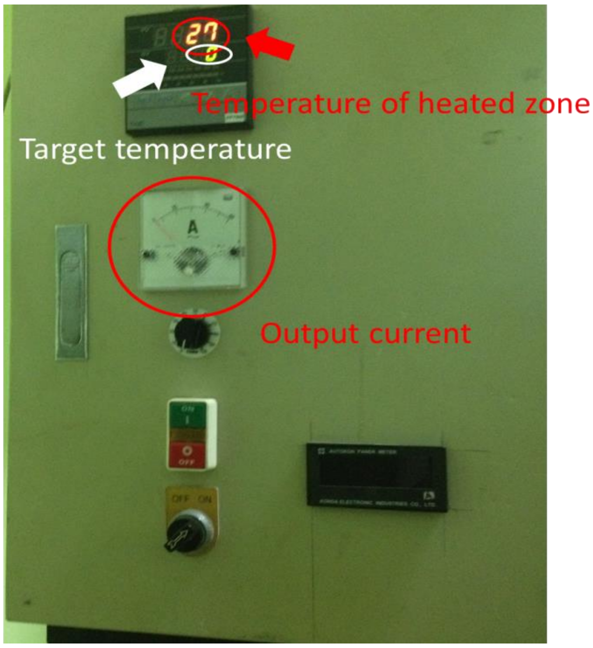

Fig. 2-11 The heating control panel, which controls output current to the heating resistors and monitor the temperature of heated zone.

2.3 Fabrication process of Si-cored Fiber

Fig. 2-12 shows the flow chart of fabrication process for the Si-cored fibers. To fabricate the Si-cored fibers, the polycrystalline Si powders (99.999 % purity) having an average size of ca. 100 μm were packed into a fused silica tube whose outer and inner diameters were 10 mm and 2 mm, respectively. One end of the fused silica tube was sealed by using oxy-hydrogen flame. Then the powder-packed fused silica tube would put on the feeding system holder so that we could control the speed of feeding appropriately. We would put the tube into high temperature furnace after silica tube was firmly fixed to the holder. The tube was drawn in the homemade drawing tower at some suitable temperature varying from 1630 to 1720℃. In this temperature range, the Si powders would melt and the fused silica tube would become softened, and then we drew the tube out of heated region to be in a fiber form as shown in Fig. 2-13. Fig. 2-14 shows a schematic illustration on how the Si-cored fibers were made through the vertical drawing process. The fluid silicon would solidify because temperature of silicon dropped dramatically when it came out of the heated region. During the drawing process the air pressure inside the tube was kept low by using a mechanical pump. Because there would be some oxygen diffused into silicon to be silica which degraded the quality of silicon during the high temperature drawing process, the vacuum pump would be employed to avoid oxidation. Furthermore, if the air were not removed, it would block the melting silicon, resulting in a discontinuous Si-cored fiber as shown in Fig. 2-15. Because the heating resistor would be oxidized easily in high temperature, the nitrogen gas purging should be executed throughout the drawing process. However, the flow rate of nitrogen should be controlled appropriately because excessive flow rate would result in fiber break fibers or heater damage.

It was found that the drawing temperature would significantly affect the crystallinities and the morphologies of the Si core. At temperature of 1580^{o}C, the Si-cored fibers were easily broken during the drawing process and the dimension of Si-cored fiber was large relative to higher temperature (1650^{o}C) as shown in Fig. 2-16. Since the melting temperature and softening point of fused silica are ca. 1732^{o}C and 1630^{o}C, respectively, the silica cladding would not become softened enough to sustain the force of drawing at 1580^{o}C. However, the silica cladding would become too soft to remain the fiber shape at excessively high temperature ca. 1730^{o}C as shown in Fig. 2-17. Conversely, the Si-cored fibers could be continuously formed and cracks in fiber be decreased substantially at 1710^{o}C as shown in Fig. 2-18. With appropriate adjustments the Si-cored fibers were found easily fabricated ca. 1650^{o}C at which temperature the Raman peaks were very close to single crystal (ca. 519 cm^{-1}); therefore, such a temperature was chosen throughout the study. Fig. 2-19 shows an optical image of Si-cored fiber after appropriate adjustment in fabrication temperature. The difference of the Raman peaks between the Si-cored fiber and a single-crystal Si wafer will be discussed later. The Si-cored fibers were drawn at a high speed of 5~12 m/min with resultant silica cladding and Si core diameters being in the range of 50-2000 μm and 10-400 μm; the parameters and results are shown in Table 2-1. Table 2-2 shows the comparison of diameter range between the reported Si-cored fiber fabrication methods and this work. Since the fibers were not flexible enough to be coiled around a spool at such diameters, they were scribed off in sections, for example, ca. 2 m each. The Si cores inside the fibers were found continuous without observable defects by removing cladding as shown in Fig. 2-20.

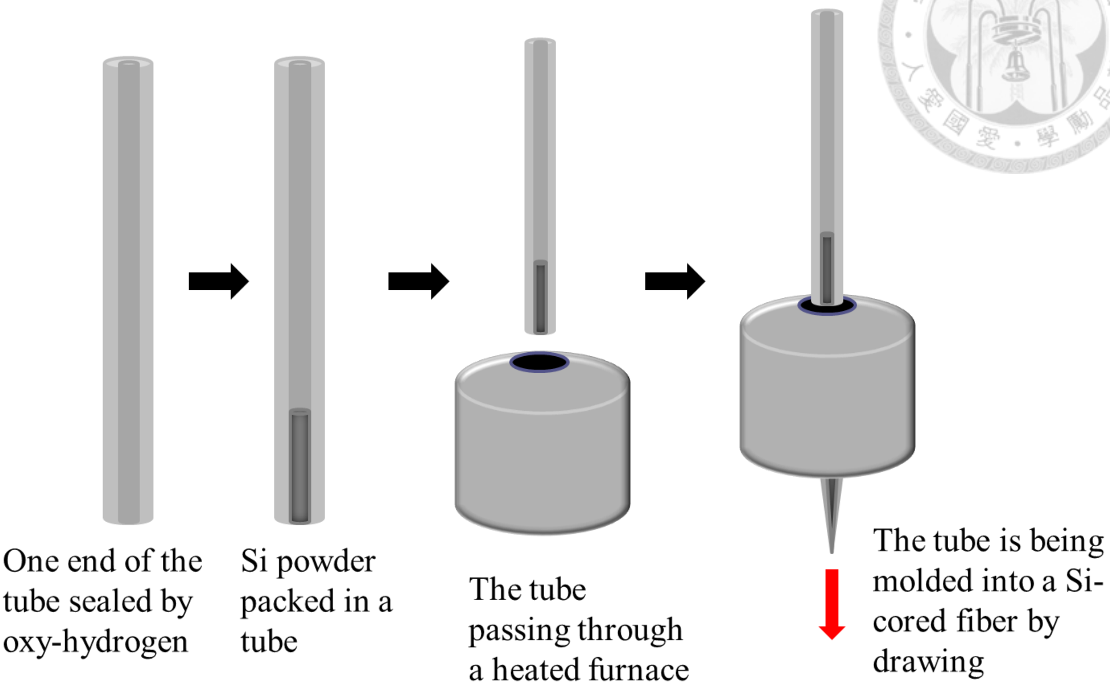

Fig. 2-12 A flow chart of fabrication process for a Si-cored fiber.

Fig. 2-13 The tube is molded into a Si-cored fiber by drawing.

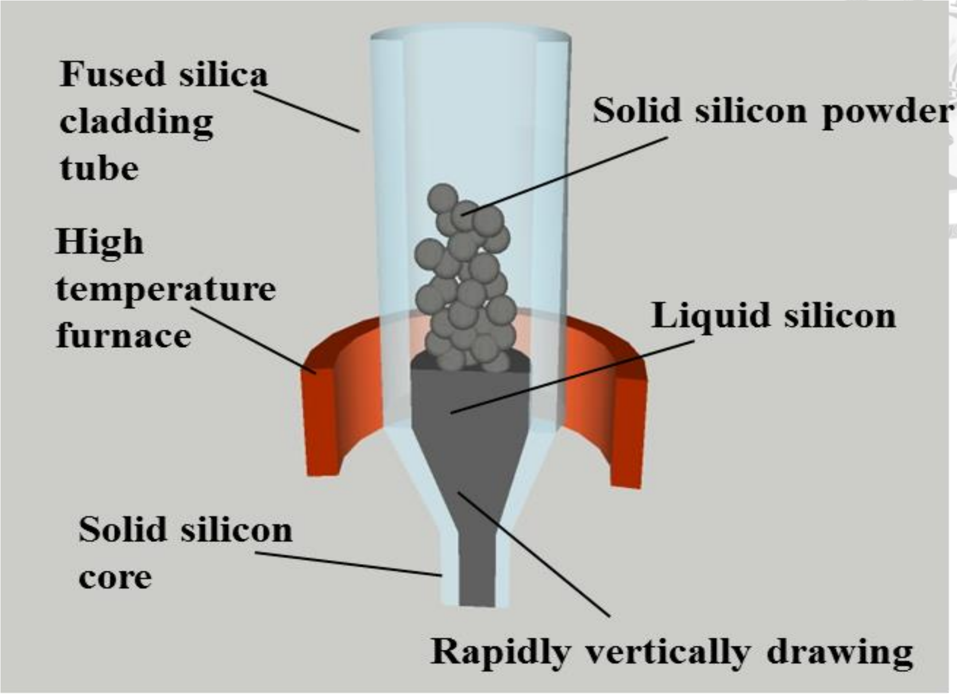

Fig. 2-14 A schematic illustration shows how the Si-cored fibers are made through the vertical drawing process.

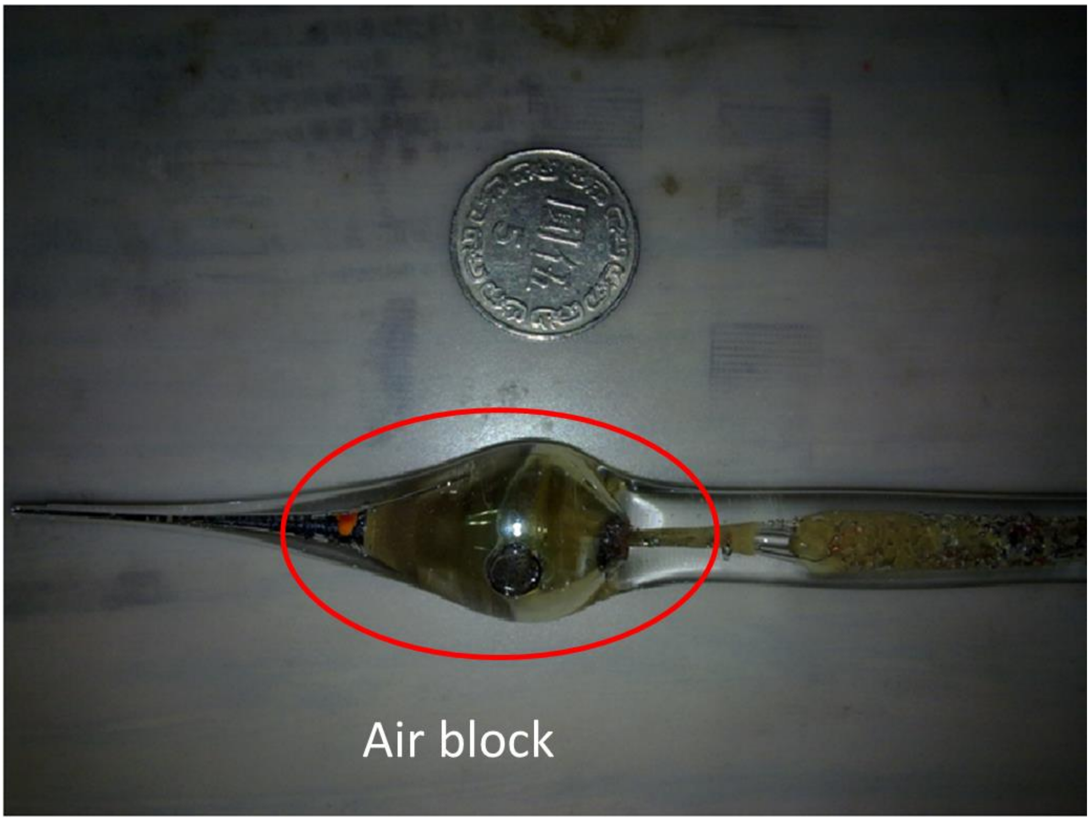

Fig. 2-15 The melt silicon is blocked by air jam.

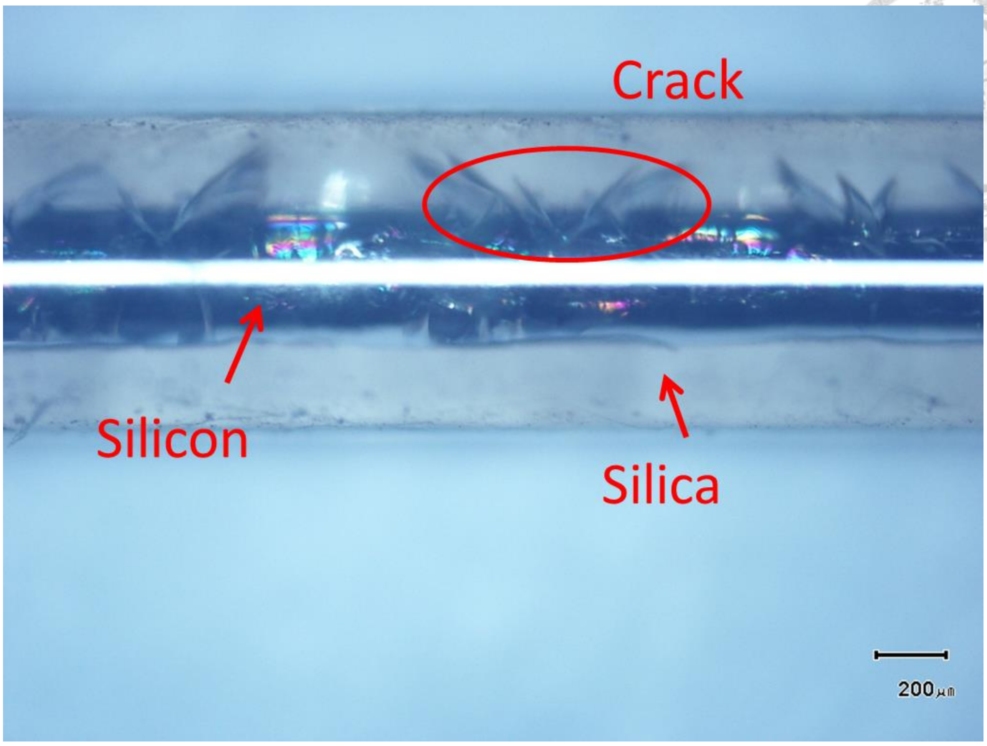

Fig. 2-16 An optical image shows that there are some cracks in Si-cored fibers.

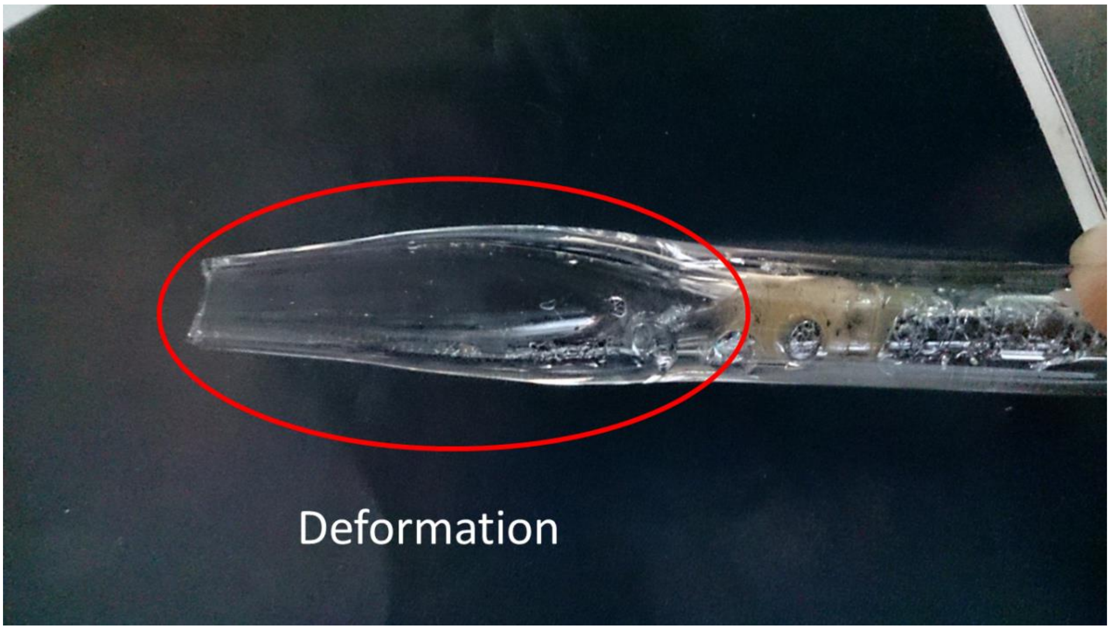

Fig. 2-17 Si-cored fibers are deformed because of too high temperature.

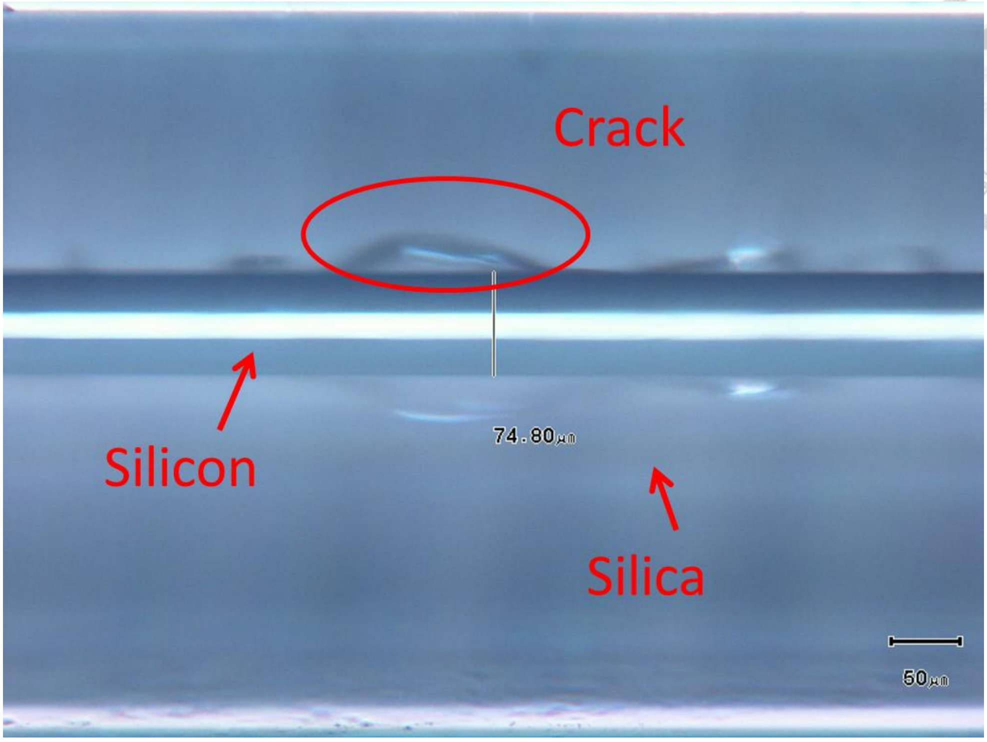

Fig. 2-18 Cracks in Si-cored fiber are decreased at higher working temperature.

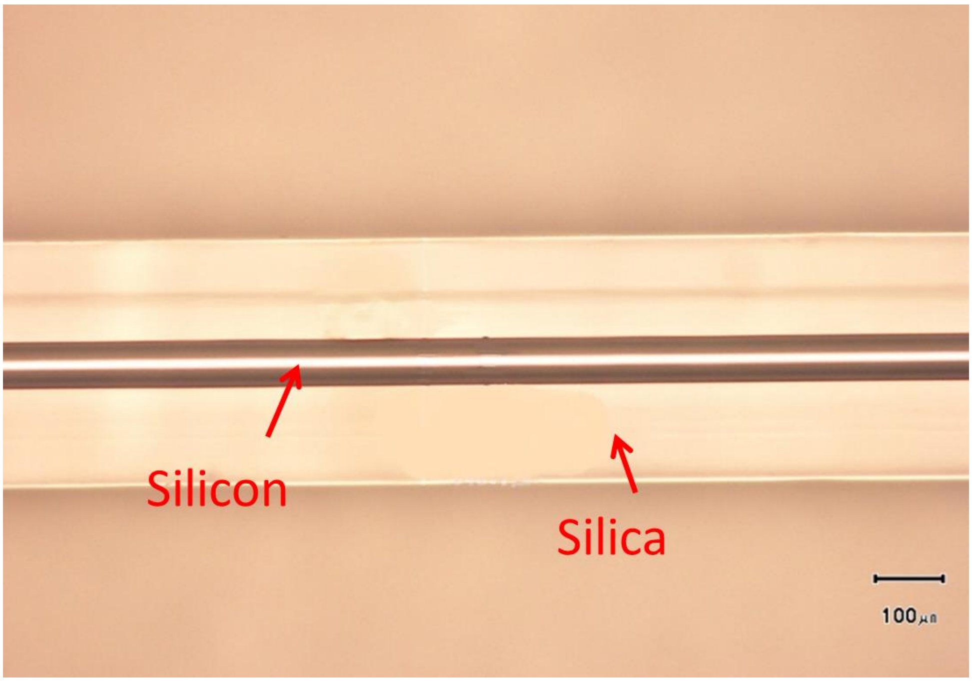

Fig. 2-19 An optical image of Si-cored fiber shows that there are no obvious cracks along fiber.

Drawing speed	Observation	Diameter of Si cored fiber	Crystallinity
Slow draw ~5 meter/min.	Serious bulging	120~400 μm	Amorphous
Fast draw ~8 meter/min.	Slight bulging	100~250 μm	Amorphous+ Polycrystalline
Faster draw ~10 meter/min	Slight bulging	50~100 μm	Single crystalline
Faster and stepped draw ~12 meter/min.	No bulging	10~50 μm	Single crystalline

Table 2-1. Si-cored drawing at different speed and the results.

Fabrication method	Cladding diameter range	Core diameters range
HPCVD	X	1~10 µm
Molten core method	600~1200µm	60~120µm
Powder-in-tube method	40~240µm	10~100µm
This work	50~2000µm	10~400µm

Table 2-2. Comparison of diameter range between the reported fabrication methods and this work.

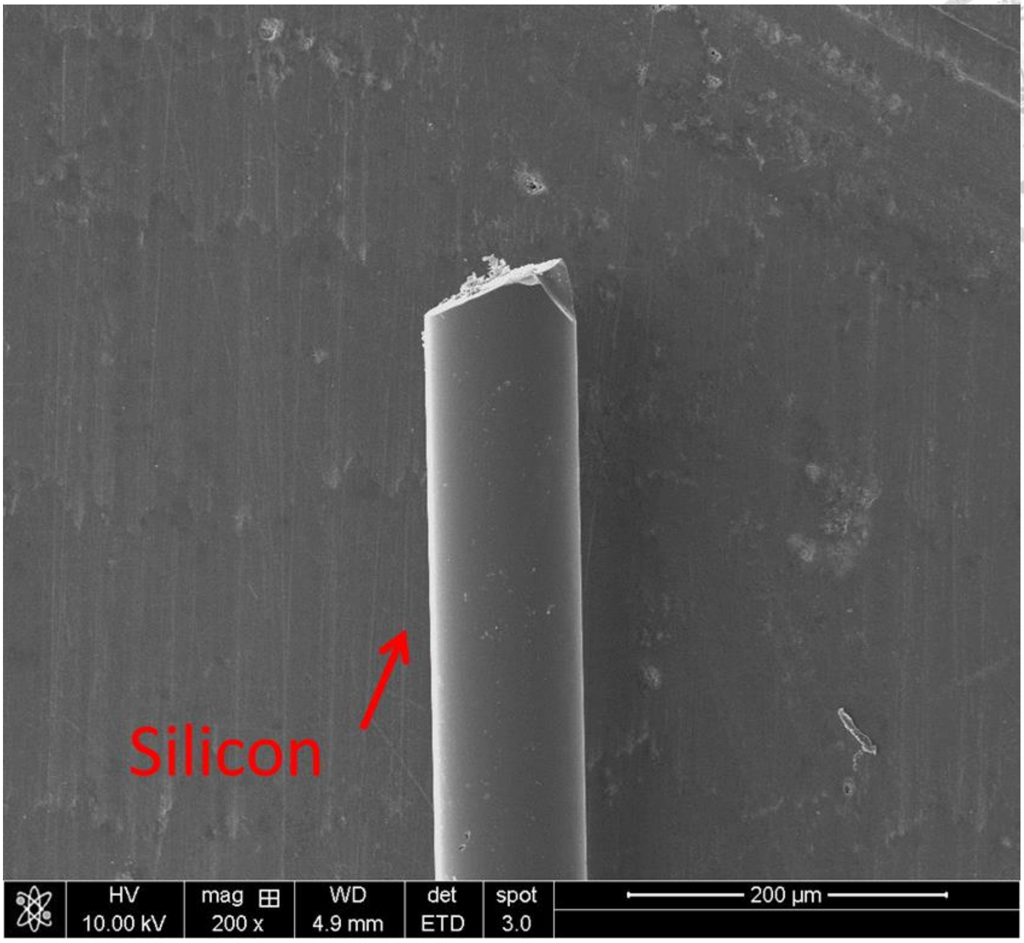

Fig. 2-20 An SEM image of Si core inside the fiber is continuous without observable defects.

Chapter 3 Characteristic of Si-cored Fibers

3.1 Material Characteristic of Si-cored Fibers

Study on Si-cored fibers is new to our group so we would compare our measured results of Si-cored fibers to the other groups who have studied this topic for many years to further improve the fabrication process. Because the electrical and optical characteristics of Si are much affected by the crystallinity of Si, we need first analyze the crystallinity of Si-cored fibers, and then measure their electrical and optical characteristics.

3.1.1 Energy-Dispersive X-ray Spectroscopy

According to [7], energy-dispersive X-ray spectroscopy (EDS, EDX, or XEDS), sometimes called energy dispersive X-ray analysis (EDXA) or energy dispersive X-ray microanalysis (EDXMA), is an analytical technique used for the elemental analysis or chemical characterization of a sample. It relies on an interaction of some source of X-ray excitation and a sample. Its characterization capabilities are due in large part to the fundamental principle that each element has a unique atomic structure allowing unique set of peaks on its X-ray emission spectrum. To stimulate the emission of characteristic X-rays from a specimen, a high-energy beam of charged particles such as electrons or protons, or a beam of X-rays, is focused into the sample being studied. At rest, an atom within the sample contains ground state (or unexcited) electrons in discrete energy levels or electron shells bound to the nucleus. The incident beam may excite an electron in an inner shell, ejecting it from the shell while creating an electron hole where the electron was. An electron from an outer, higher-energy shell then fills the hole, and the difference in energy between the higher-energy shell and the lower energy shell may be released in the form of an X-ray. The number and energy of the X-rays emitted from a specimen can be measured by an energy-dispersive spectrometer. As the energy of the X-rays is characteristic of the difference in energy between the two shells, and of the atomic structure of the element from which they were emitted, this allows the elemental composition of the specimen to be measured.

Because the fabrication of Si-cored fibers was executed at extreme high temperature, the probability of oxidation would considerably increase. If the oxygen diffused into silicon during the drawing process, the oxygen presented in the core must be precipitated into oxide because the solubility limit of oxygen is low [3]. To investigate the oxygen diffusion condition of our Si-cored fibers, EDS was used to analyze the elemental composition of Si-cored fibers. Fig. 3-1 shows the EDS measurement of Si-cored fiber by scanning along its radial direction. Fig. 3-2 shows about 10~20 % oxygen was diffused into the silicon core, which could be improved by employing a vacuum pump. Because of employing a vacuum pump, the discontinuity of liquid silicon flow which caused by air in tube could be eliminated. And the oxygen molecules could be reduced at the same time. Fig. 3-3 shows the content of oxygen in the silicon core was considerably decreased after we employed the vacuum pump.

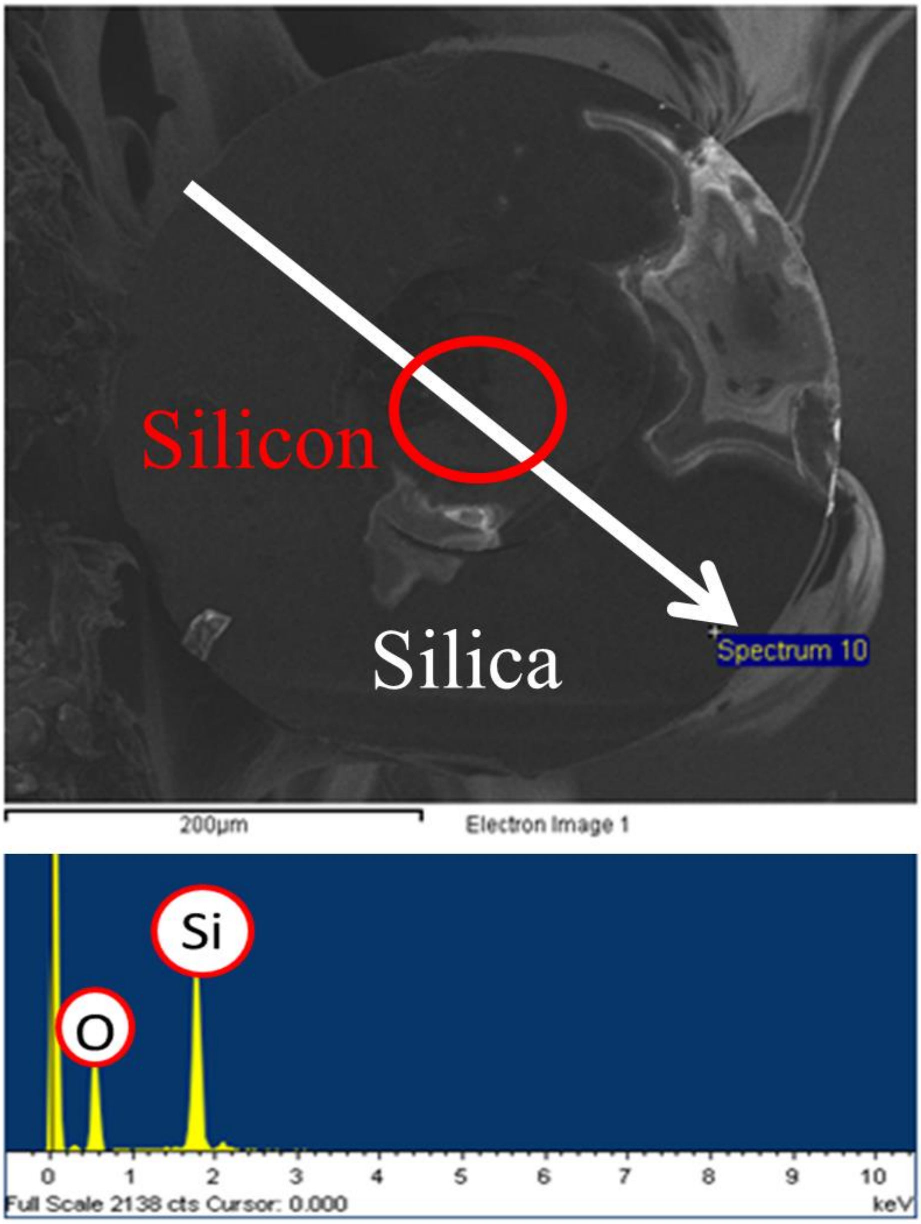

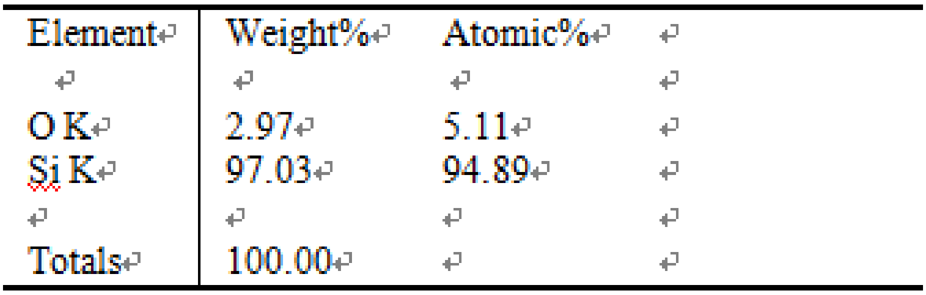

Element	Weight%	Atomic%
O K	2.97	5.11
Si K	97.03	94.89
Totals	100.00	

Fig. 3-1 EDS measurement of the Si-cored fiber by scanning along its radial direction and the weight percentage of its elements are obtained.

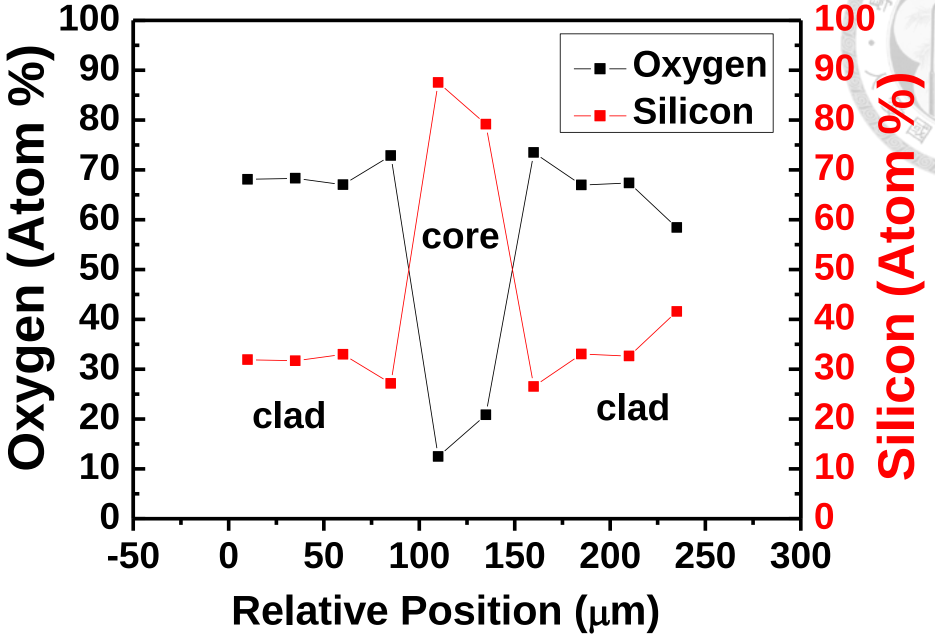

Fig. 3-2 Distributions of Si and O elements across the Si-cored optical fiber without employing the vacuum pump in drawing process.

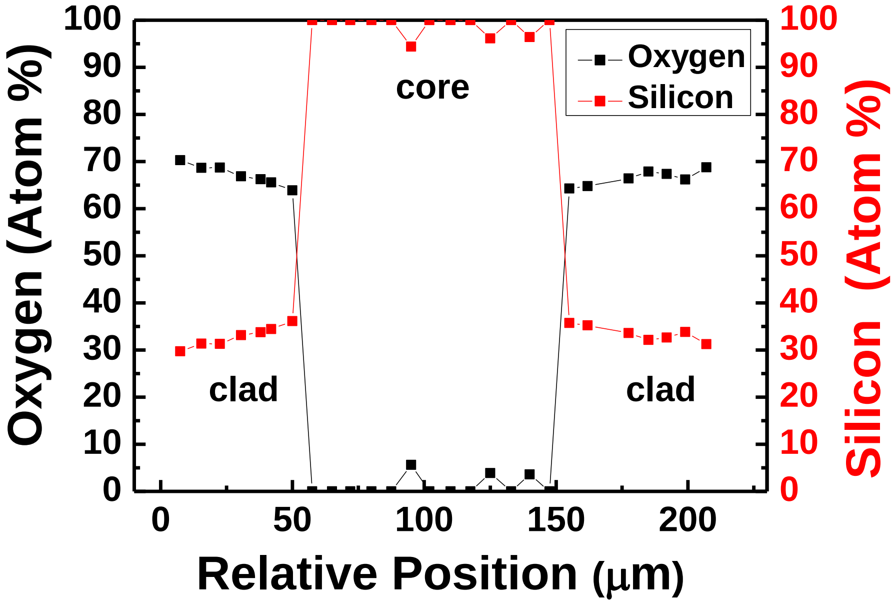

Fig. 3-3 Distributions of Si and O elements across the Si-cored optical fiber after employing the vacuum pump in drawing process.

3.1.2 Raman Spectroscopy

According to [8], Raman spectroscopy is a spectroscopic technique used to observe vibrational, rotational, and other low-frequency modes in a system. It relies on inelastic scattering, or Raman scattering, of monochromatic light, usually from a laser in the visible, near infrared, or near ultraviolet range. The laser light interacts with molecular vibrations, phonons or other excitations in the system, resulting in the energy of the laser photons being shifted up or down. The shift in energy gives information about the vibrational modes in the system. Infrared spectroscopy yields similar, but complementary, information. Typically, a sample is illuminated with a laser beam. Electromagnetic radiation from the illuminated spot is collected with a lens and sent through a monochromator. Elastic scattered radiation at the wavelength corresponding to the laser line (Rayleigh scattering) is filtered out, while the rest of the collected light is dispersed onto a detector by either a notch filter or a band pass filter.

Spontaneous Raman scattering is typically very weak, and as a result the main difficulty of Raman spectroscopy is separating the weak inelastically scattered light from the intense Rayleigh scattered laser light. The energy-level diagram of Raman signal is shown in Fig. 3-4 Historically, Raman spectrometers used holographic gratings and multiple dispersion stages to achieve a high degree of laser rejection. In the past, photomultipliers were the detectors of choice for dispersive Raman setups, which resulted in long acquisition times. However, modern instrumentation almost universally employs notch or edge filters for laser rejection and spectrographs either axial transmissive, Czerny–Turner monochromator, or Fourier transform spectroscopy based, and CCD detectors.

To study further the material properties of Si core, the silica cladding of a Si-cored fiber was removed by using buffered hydrofluoric acid solution. Fig. 3-5 shows the electron microscope (SEM) image of a cylindrical Si fiber. Such a fiber without cladding is henceforth called Si fiber. Such a cylindrical shape of the Si fiber is the evidence that the polycrystalline Si powders were completely melted in the tube during the drawing process. Fig. 3-6 shows the Raman spectra of the n-type polycrystalline Si powders and Si fiber. After Si powders were melted and formed as Si fibers, the peak position (512.39 cm^{-1}) of the transverse optical (TO) mode of the Si powder shifted to the wavenumber of (520.85 cm^{-1}). It is apparent that transformation of crystallinity of Si was resulted from drawing process. Fig. 3-7 shows the Raman spectra of the single-crystal Si wafer, the n-type Si-cored fiber (core/cladding diameters = 100/500 μm) and the Si fiber. Note that the Raman peaks of the reference single-crystal Si wafer and the Si-cored fiber are located at 520.85 cm^{-1} and 518.69 cm^{-1}, respectively. It is apparent that the peak position (518.69 cm^{-1}) of the transverse optical (TO) mode of the Si-cored fiber is close to that of single-crystal Si (520.85 cm^{-1}). After the silica cladding was removed to unveil the Si core, the TO mode shifted to the wavenumber of 520.85 cm^{-1}, which is coincident with that of the reference single-crystal Si. It has been reported that the Raman peak of single-crystal Si when subjected tensile stress would shift to shorter wavenumbers [8]. Therefore the amount of wavenumber short-shift, about 2.16 cm^{-1}, in the Si-core fiber indicates that the Si core is under a tensile stress.

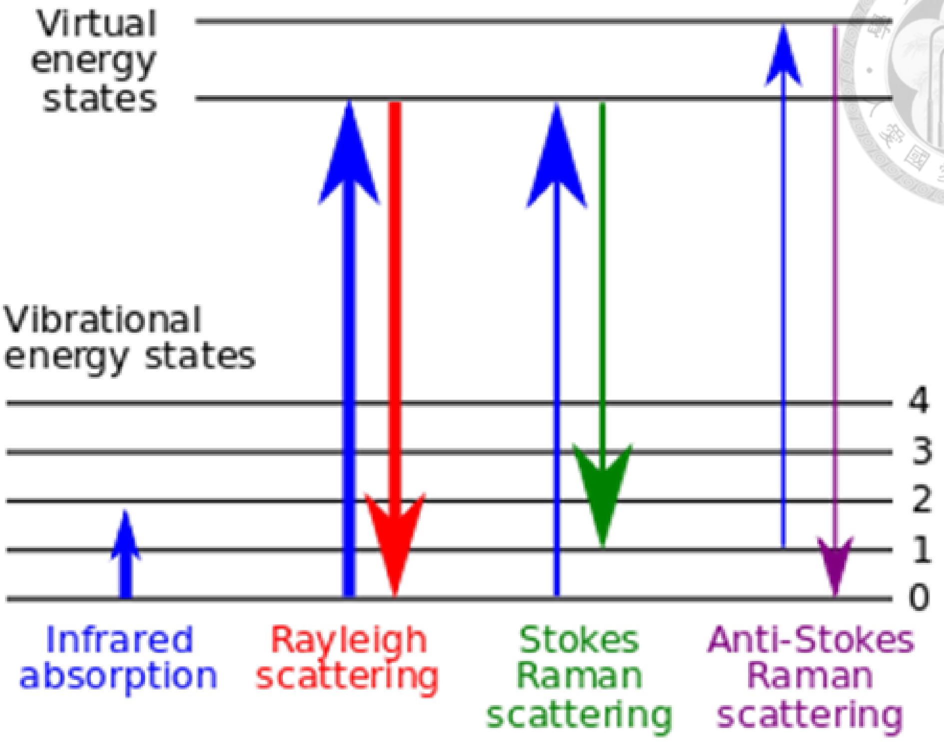

Fig. 3-4 An energy-level diagram of Raman signal. [8]

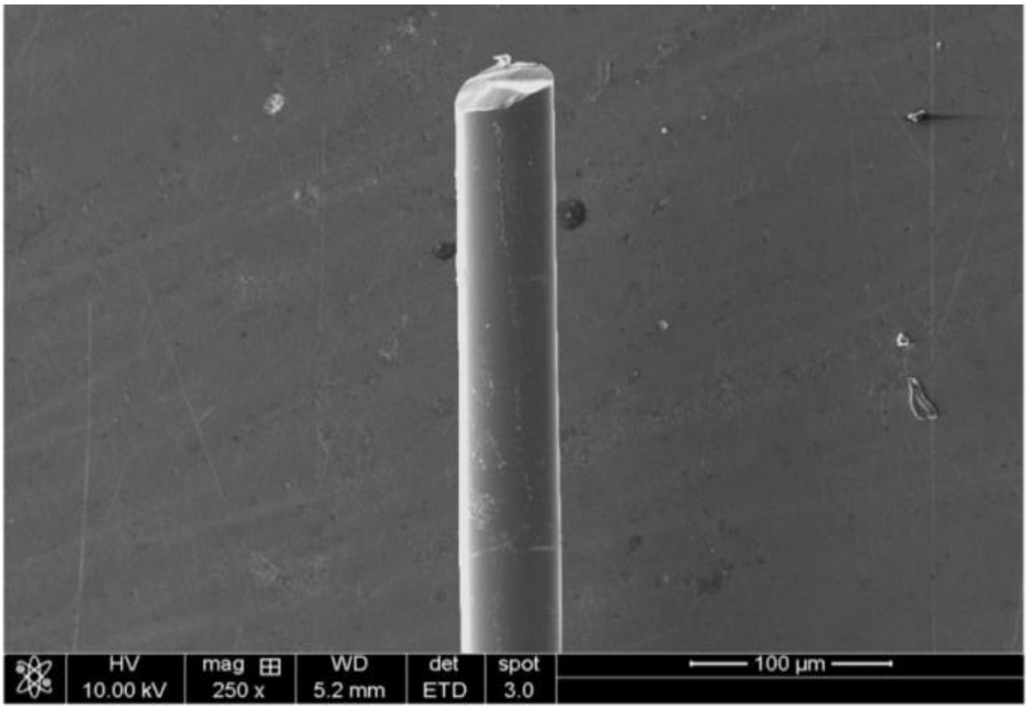

Fig. 3-5 An SEM image of Si fiber.

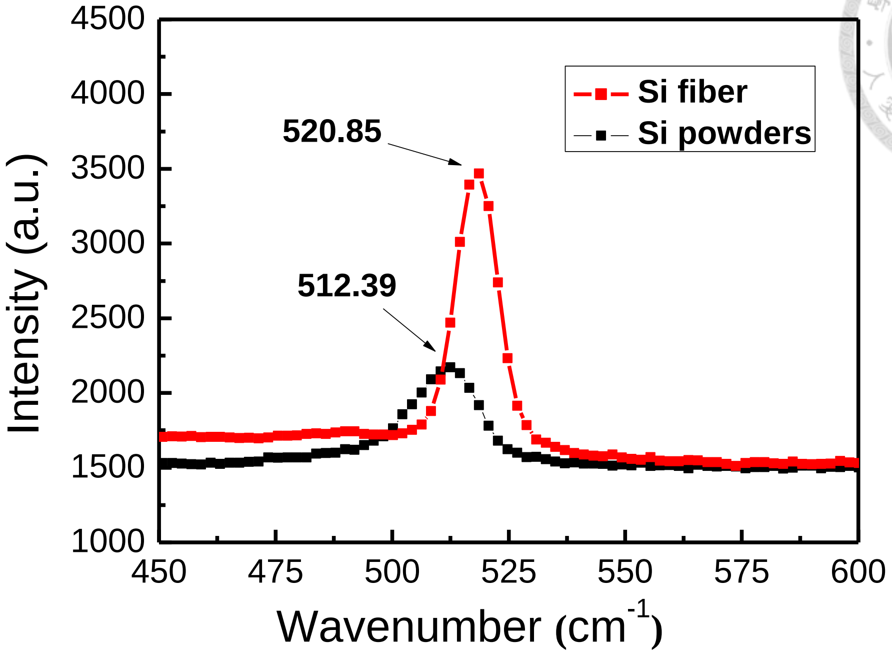

Fig. 3-6 Raman spectra of the intrinsic polycrystalline Si powder and a Si fiber.

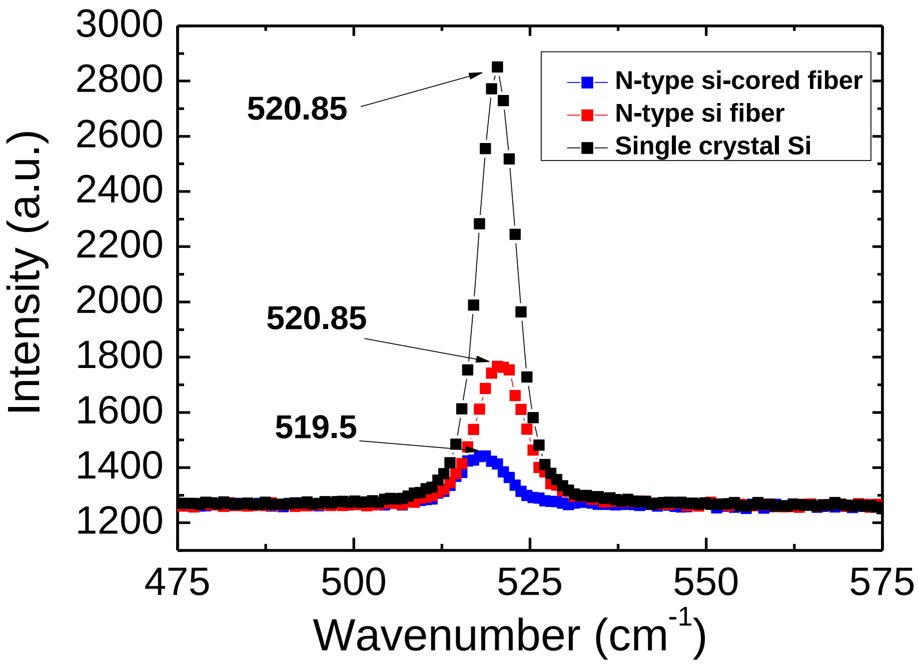

Fig. 3-7 Raman spectrum of n-type Si-cored fiber, Si fiber, and single crystal wafer.

3.2 Electrical Measurement of Si-cored Fibers

To ensure that the doped concentration of Si was not changed after drawing process in which Si powders were melted at high temperature. The current-voltage (I-V) characteristics of different types of doped Si-cored fibers were measured to find the doped concentrations of Si-cored fibers. To measure the I-V characteristics of Si-cored fibers, the ohmic electrodes should be fabricated in advance. Considering the work function of Si, we used Ag paste to serve to as ohmic electrode material. Fig. 3-8 shows the schematic diagram for characteristics I-V measurement of Si cored fibers. The Ag paste should be sintered at 500 ^{o}C to volatilize the solvent in the paste to be ohmic contact. Fig. 3-9 shows the I-V characteristics of Si-cored fibers before sintering (a) and after sintering (b). The I-V characteristics of intrinsic, n-type and p-type Si-cored fibers are shown in Fig. 3-10 (a), (b), (c). It is apparent that the resistivity of intrinsic Si-cored fibers is higher than n-typed and p-typed doped. According to the equation as follows

$$R = \rho \times \frac{L}{A} \tag{3-1}$$

where R is the resistance of Si fiber; ρ is the resistivity of Si fiber; L is the length of Si fiber; A is the cross section area of Si fiber. We could calculate the resistance from the I-V diagram and measure the length and cross section area of Si fiber and thus the resistivity could be obtained. The resistivity is defined as follows

$$\rho = \frac{1}{q \times [N_D \times \mu_n + N_A \times \mu_p]} \tag{3-2}$$

where q is the elementary charge; N_D and N_A are concentration of donor and acceptor, respectively; μ_n and μ_p are drift mobility of electron and hole. Therefore the N_D and N_A can be expressed as follows

$$N_D = \frac{1}{q \times \mu_n \times R \times A} \qquad N_A = \frac{1}{q \times \mu_p \times R \times A} \tag{3-3}$$

According to the diagram of electron drift mobility versus donor density and hole drift mobility versus acceptor at 300K [11] as shown in Fig. 3-11, we used the doped concentration of n-type and p-type Si powders to substitute in Fig. 3-11 so the drift mobility could be obtained and then substituted in Eq. 3-3 to calculate the doped concentration of n-type and p-type Si-cored fibers. To ensure that is there some inhomogeneous doped condition in Si-cored fiber after drawing process, we measured the resistant of Si-cored fibers under various lengths of Si-cored fibers. Fig. 3-12 shows the resistance of Si-cored fibers linearly increased with measured length of Si-cored fibers. The results showed the consistency of electrical performance of axial Si-cored fibers, so we could speculate the impurities were well distributed in Si-cored fibers even though these fibers were fabricated under the high temperature drawing process.

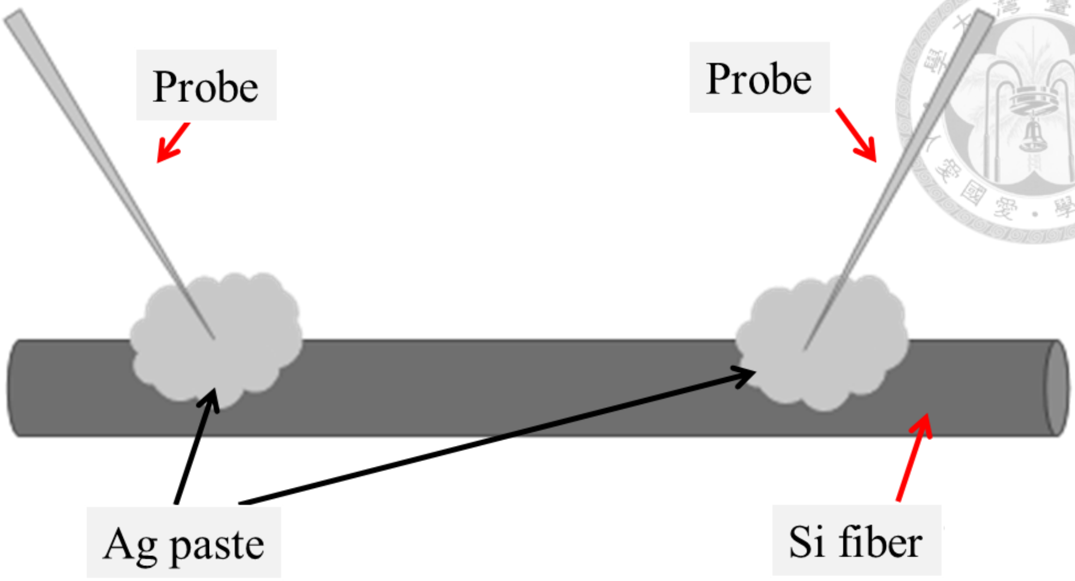

Fig. 3-8 A schematic of measurement of I-V characteristics of Si-cored fibers.

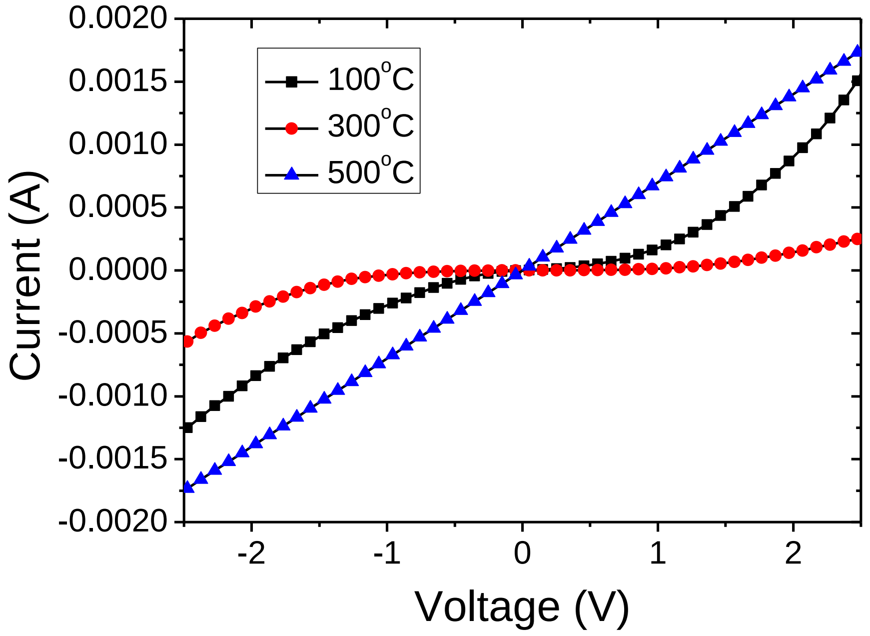

Fig 3-9 The I-V characteristics of Si-cored fibers sintered at different temperature.

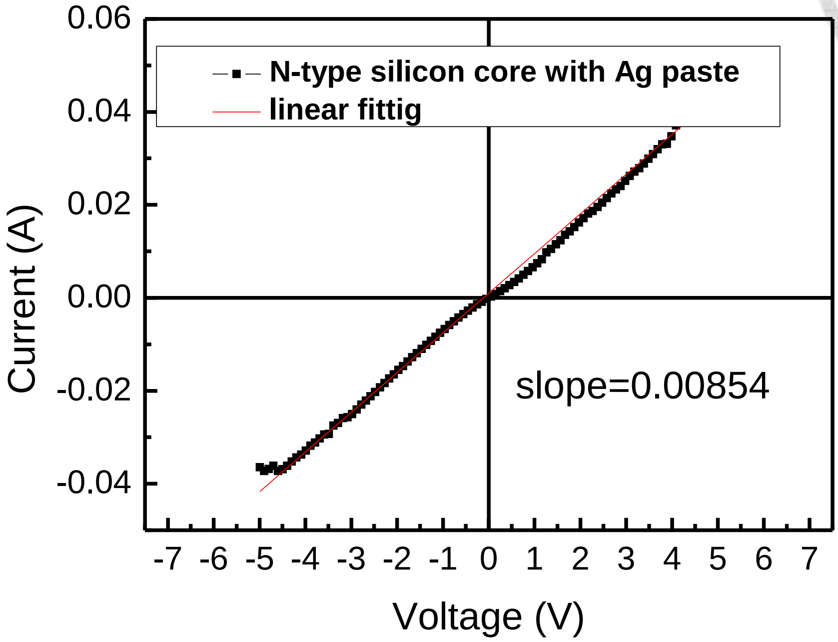
N-type silicon core with Ag paste
linear fittig
slope=0.00854
Current (A)
0.06
0.04
0.02
0.00
-0.02
-0.04
Voltage (V)
-7
-6
-5
-4
-3
-2
-1
0
1
2
3
4
5
6
7

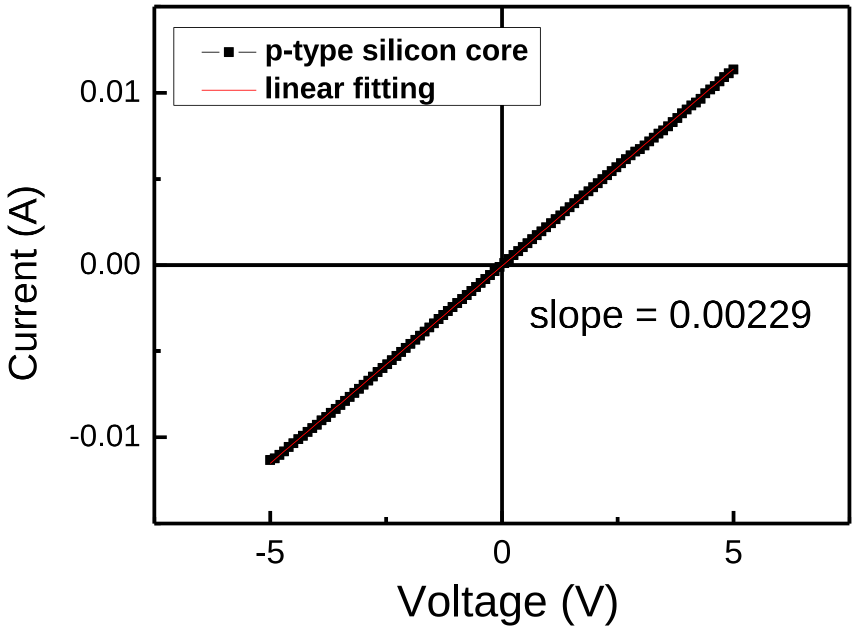
p-type silicon core
linear fitting
slope = 0.00229
Current (A)
0.01
0.00
-0.01
Voltage (V)
-5
0
5

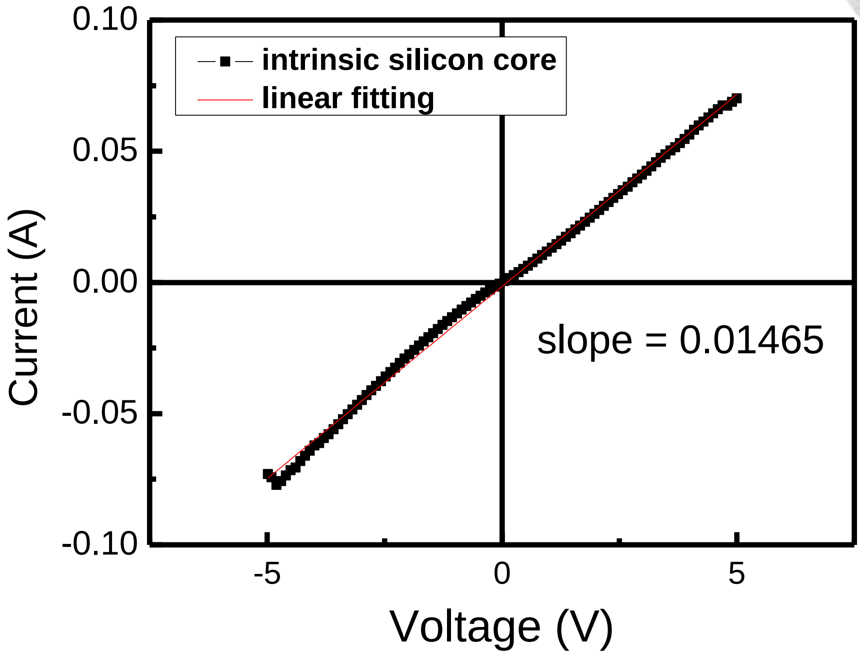

Fig. 3-10 The I-V characteristics of (a) intrinsic, (b) n-type and (c) p-type Si-cored fibers.

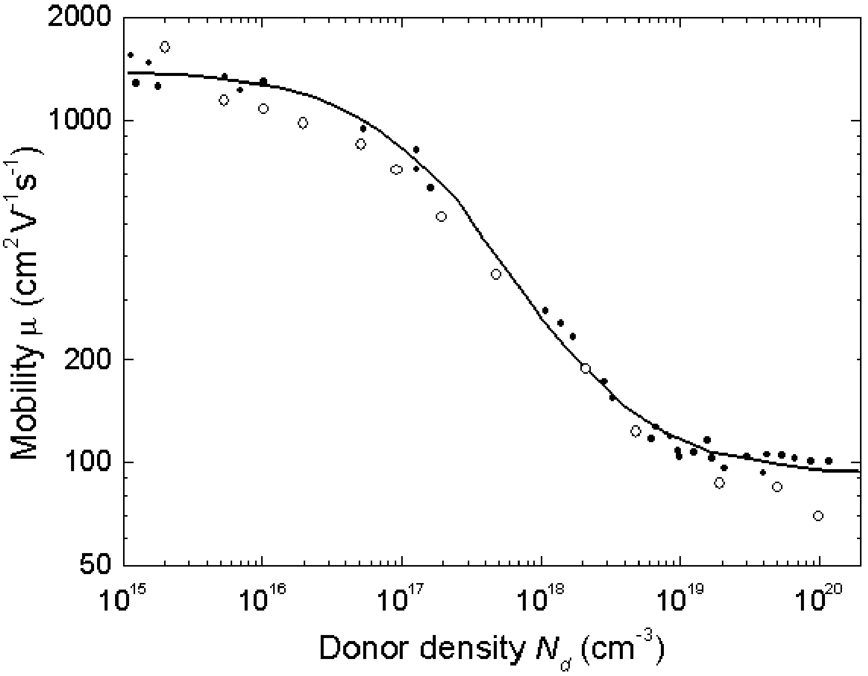

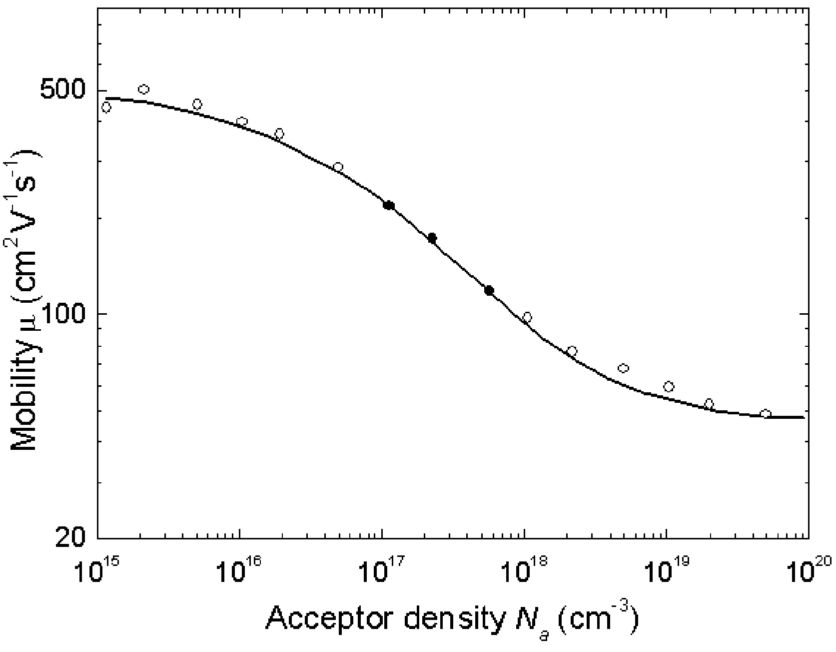

Fig. 3-11 Donor (a) and acceptor (b) density in silicon versus mobility where open and closed circles are reported by Irvin and Mousty et al, respectively [18].

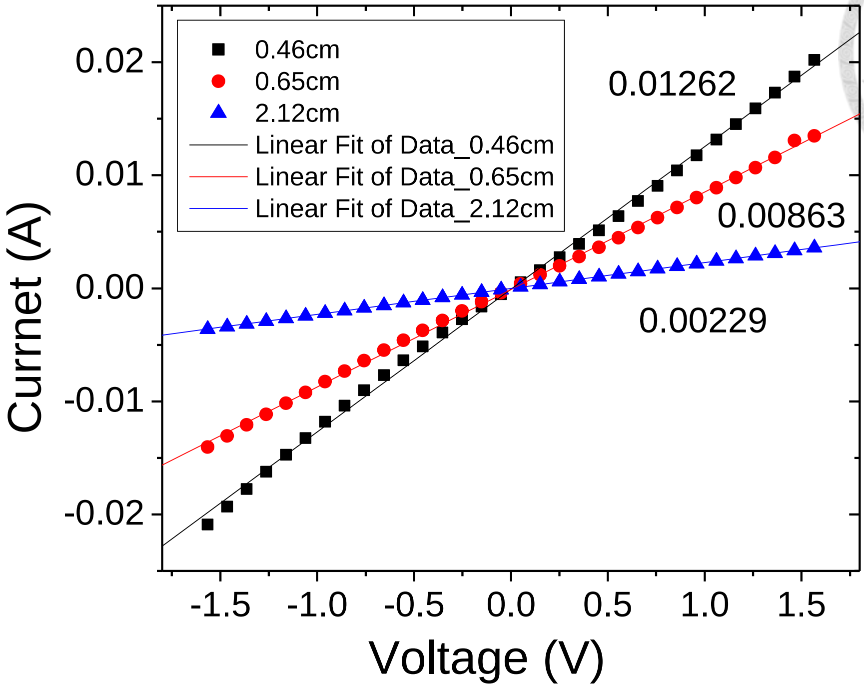

Fig. 3-12 The I-V characteristics of Si fiber in different lengths.

3.3 Optical Characteristics of Si-cored Fibers

To study the waveguide performance of Si-cored fibers, we measured the transmission losses of the Si-cored fibers and the measurement setup is shown in Fig. 3-13. Notable contributors for transmission loss may be cracks, grain boundaries (poly-crystallinity), surface roughness, longitudinal perturbations, and impurity [12]. The cut-back method was adopted for the measurement in the wavelength regime from 1520 to 1560 nm. Light was launched from a tunable laser diode through a lead-in fiber into a Si-cored fiber. The optical coupling was monitored by using a charge-coupled device (CCD) to ensure that the light was properly delivered to the Si-cored fiber. The transmitted light was then collected by a power meter. Fig. 3-14 shows that the measured transmission attenuation of core diameter range from 100 to 200 μm is ca. 0.3 to 0.4 dB/cm and range from 20 to 100 μm is ca. 0.6 to 1.0 dB/cm in the wavelength regime from 1520 to 1560 nm. The error bar is resulted from the flatness on the end face of fiber during the cut-back process and can be further improved. Even so, as summarized in Table 3-1 the Si-cored fibers made by this method possess much lower transmission losses as compared to the losses made by the other methods, usually ranging from 1.7 to 9.7 dB/cm in the optical communication regimes around 1300 or 1550 nm. Such low transmission losses are contributed to the almost perfect, single-crystal Si core.

To further investigate characteristic waveguiding of the Si core, the cladding of Si-cored fibers was removed by using buffered hydrofluoric acid solution to be Si fiber. Because the dimension of Si fibers is too small to measure transmission loss by cut-back method, we used the side coupling method instead. Fig. 3-15 shows a schematic diagram of side coupling method. A micro silica fiber taper which would attach to Si fiber was served as a lead-in fiber by using evanescent fields. Fig. 3-16 shows the silica fiber taper contacted the Si fiber in its midsection, and the emission output was detected from the end of Si fiber by a photodetector. The propagation length would change by moving the fiber taper slowly from one side to the other so the intensity of output light from end of Si fiber changed with coupling positions. Fig. 3-17 shows the measurement results of transmission attenuation of Si diameter range from 8 to 15 μm is ca. 8 and 11 dB/cm. The different transmission losses between Si-cored fibers and Si fibers could be caused by the different dimension and considerable variability of refractive index of cladding from silica to air.

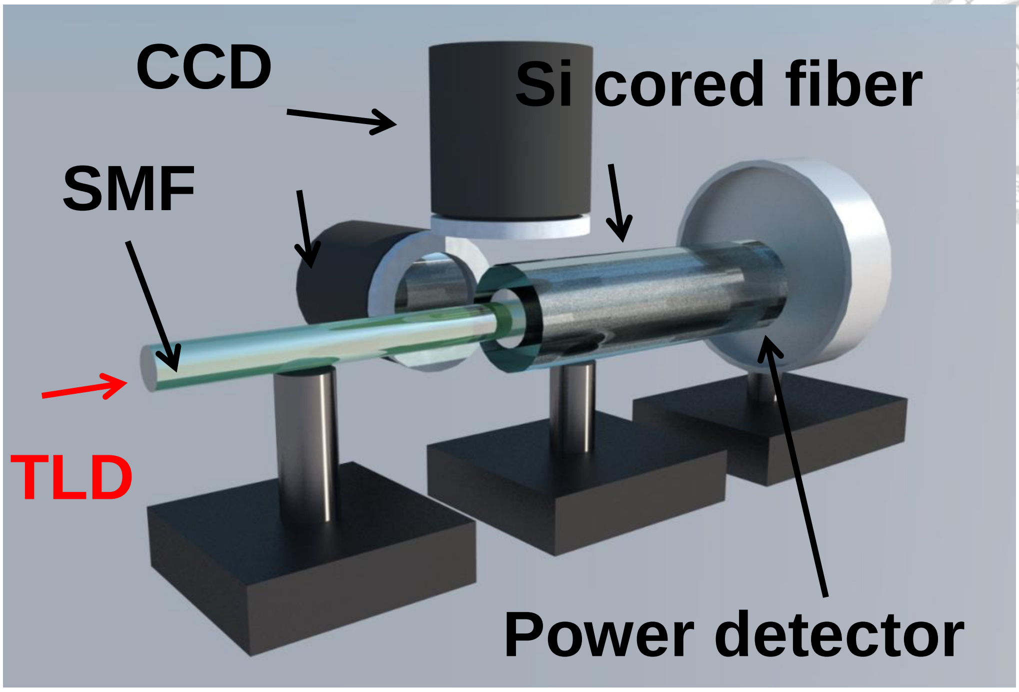

(a)

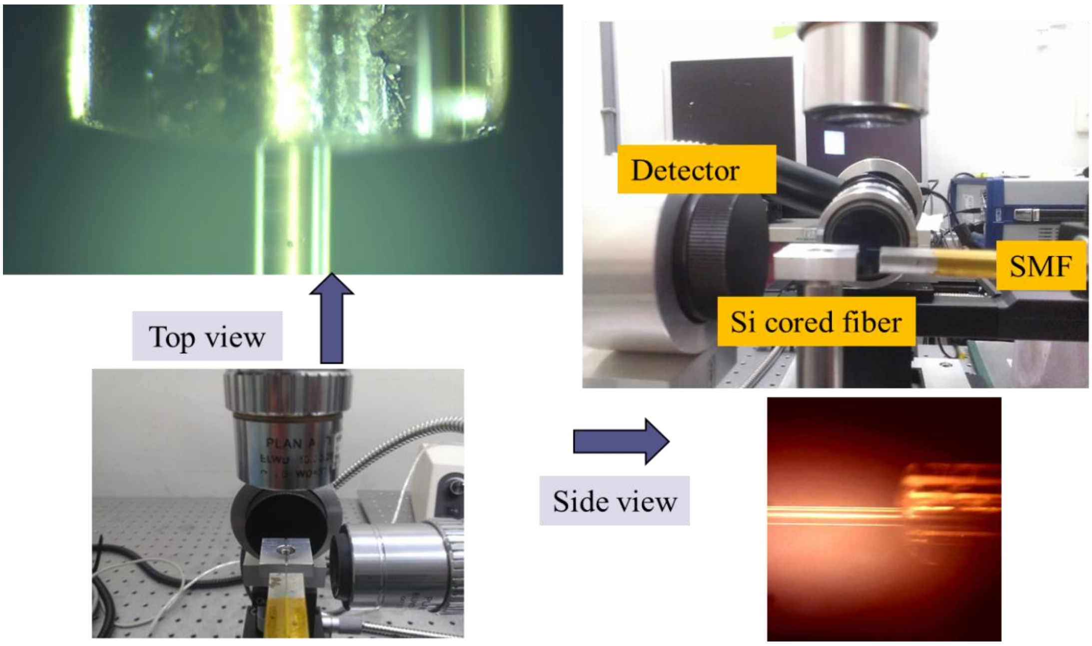

(b)

Fig. 3-13 (a) A schematic setup for transmission loss measurement; TLD: tunable laser diode, SMF: single-mode fiber. (b) Photograph of the transmission loss measurement setup.

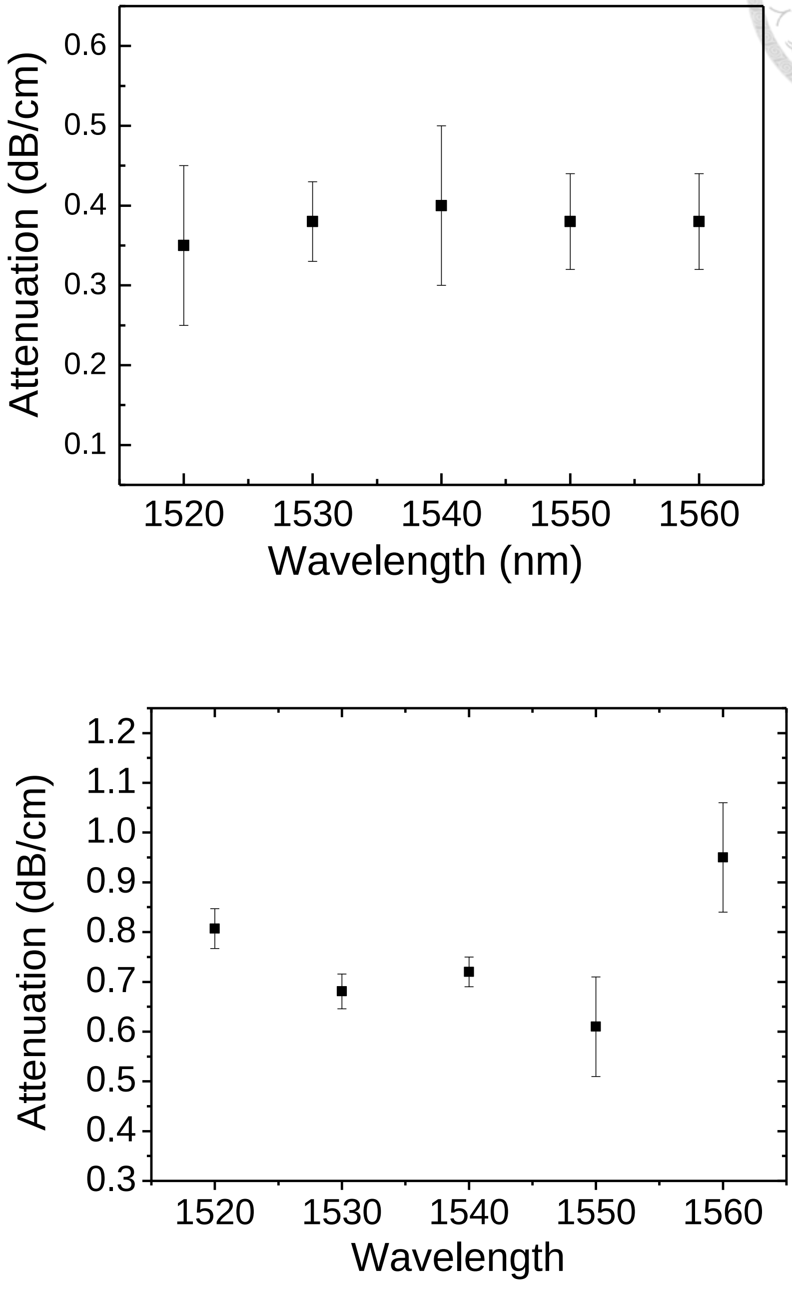

Fig. 3-14 The measured transmission losses of Si-cored fibers (a) diameter ranging from 100 to 200 μm (b) diameter ranging from 20 to 100μm in the wavelength regime from 1520 to 1560 nm.

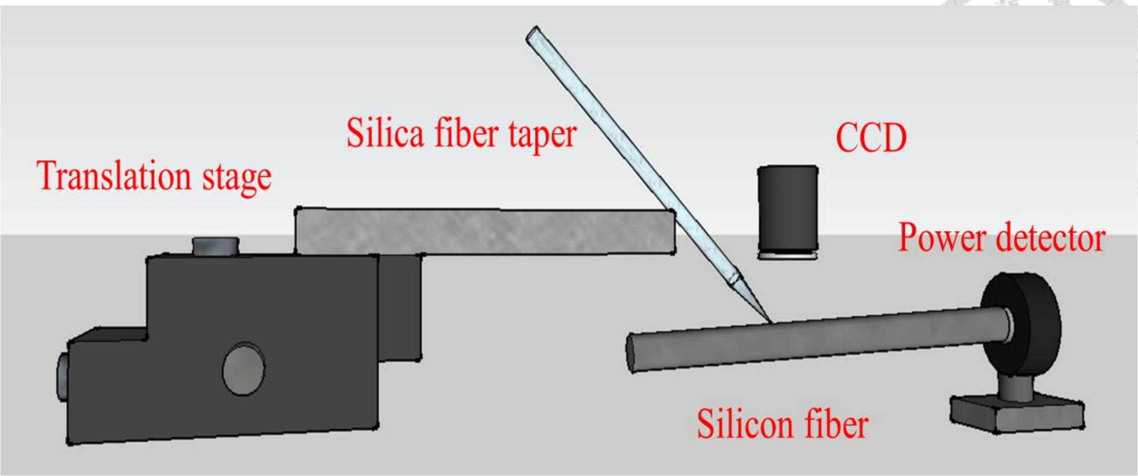

Fig. 3-15 A Schematic setup for side coupling method.

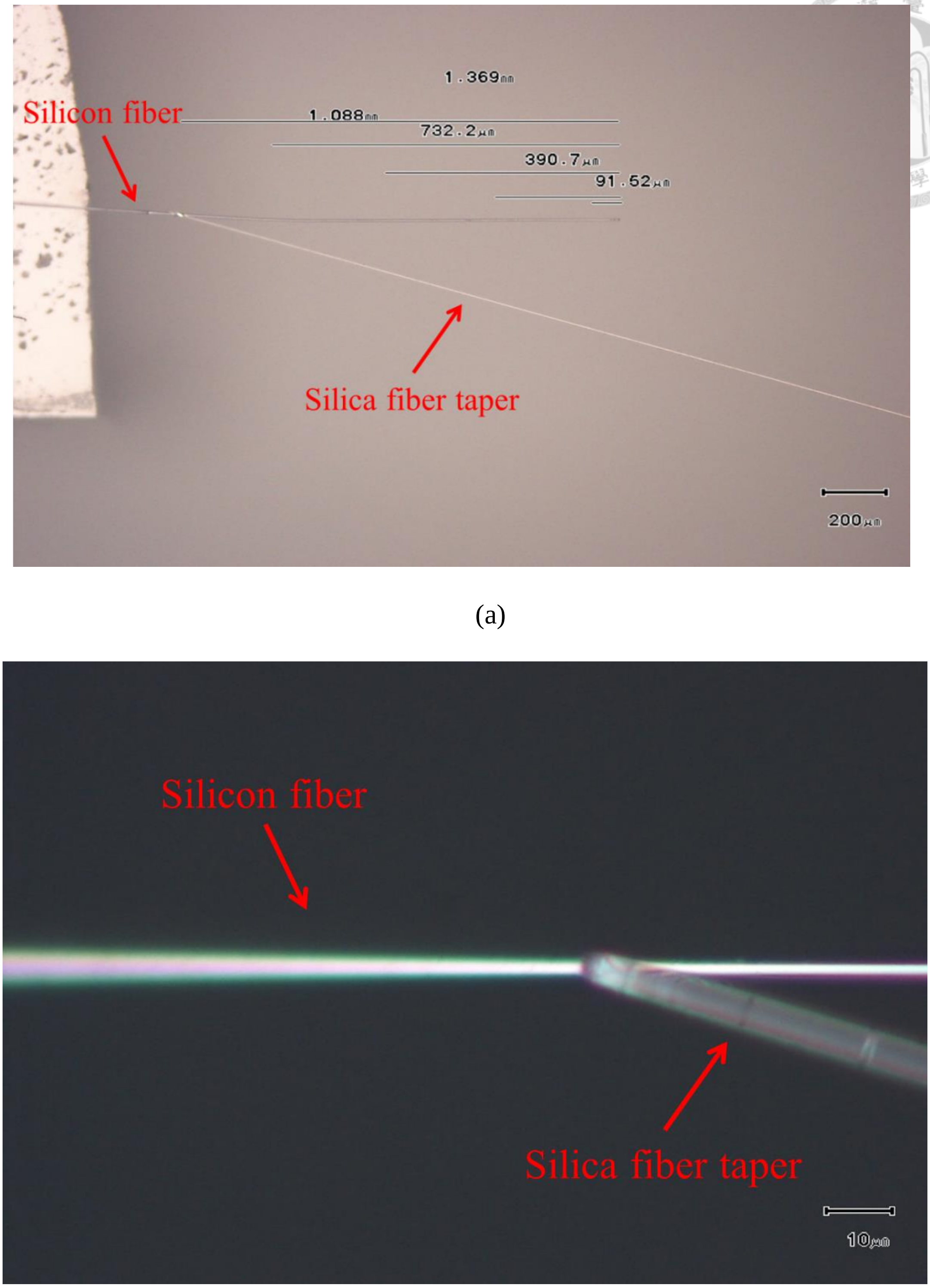

(a)

(b)

Fig. 3-16 (a) Optical microscope image of measuring the transmission loss by side coupling method (b) after zooming in from (a).

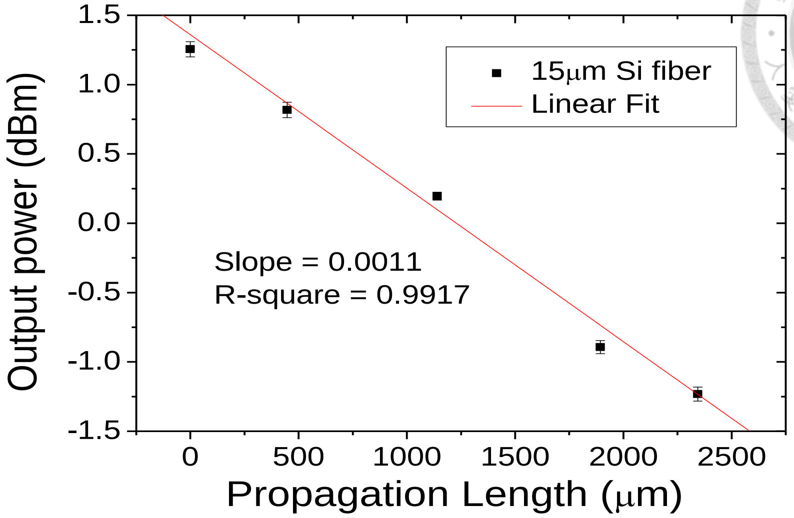

(a)

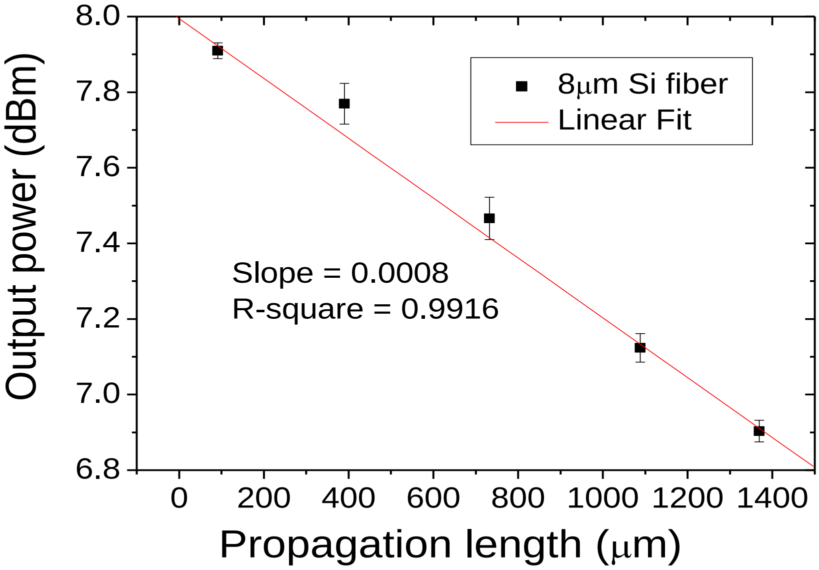

(b)

Fig. 3-17 The measurement of transmission loss of Si fiber diameter of (a)15μm and (b) 8μm by side coupling method.

Source Material	Fabrication Method	Crystallinity of Fiber Core	Transmission Loss (dB/cm) in measured wavelength	Core Diameter (μm)	Reference
Precursors for a-Si:H	HPCVD	Amorphous	1.73 in 1.55 μm	6	[17]
Precursors for Si	HPCVD	Amorphous	3 in 1.55 μm	5.6	[10]
Single crystal Si rod	Molten core drawing	Highly crystalline	2.7 in 1.306 μm, 0.043 in 2.936 μm	50, 150	[3]
Single crystal Si rod	Molten core drawing	Single crystalline 4–5 mm long	7.8 in 1.3 μm	100	[2]
Single crystal Si powder	Powder in tube	Highly crystalline	9.7 in 1.3 μm	200	[4]
Poly-crystalline Si powder	**Molten core drawing**	**Single crystalline in meters**	**0.3-0.4 in 1.52-1.56 μm**	**40-400**	**This work**

Table 3-1. Comparison between the reported Si-cored fibers and this work in terms of source materials, fabrication methods, crystallinity of fiber cores, transmission losses and core diameters.

3.4 Splicing of Si-cored Fiber

The splicing of Si-cored fiber and Si microfiber was carried out by using an arc discharge device, which was placed on a manipulation system and fitted under an optical microscope as schematically shown in Fig. 3-18 (a). The tungsten carbide (WC) electrodes could withstand high temperature ~1700℃ during discharging. Depending on the diameters of microfibers, parameters such as the separation distance of electrode tips, applied current and relative positioning needed to be optimized to obtain a stable arc as shown in Fig. 3-18 (b). Before arc splicing two fibers were first attached to each other by manipulating translation stage. A proper overlapping length and alignment within the arc discharge region was needed for good attachment. It was observed that the two Si-cored fibers were connected straight to each other and two Si microfibers were overlapped each other as shown in Fig 3-19 (a) and 3-20 (a). However, such connection was easily affected by other larger forces such as those induced by manual movement, resulting in the change of coupling length and unstable output power, which was unacceptable in practical applications. Afterwards an arc discharge was applied to the overlapping region with suitable current and duration. Note that too high current would break the weak link between two Si microfibers, and too low current could not offer sufficient heat to melt Si microfibers. During the arc discharging, the two Si microfibers melted to become one as well as Si-cored fibers. Fig. 3-19 (b) shows a photograph of a spliced Si cored fiber and Fig. 3-20 (b) shows a photograph of a spliced Si microfiber, and note that the overlap region is still thicker than both sides. The arc splicing made two Si microfibers strongly fixed together and consequently output power became more stable as compared to those obtained by evanescent coupling. The fusion loss of Si fibers was measured by side coupling method. The measurement result was shown in Fig. 3-21. However, the fusion of Si cored fibers could not measure by side coupling method because of the difference of structure between Si fibers and Si-cored fibers. We measured variety of output power before and after fusion of Si-cored fibers. Finally, we demonstrated the splicing of Si-cored fiber with single mode fiber. It was observed that the Si-cored fiber and single mode fiber were aligned each other as shown in Fig. 3-22. During the arc discharging, the Si-cored fiber would radiate due to Black-body radiation which was caused by object in high temperature. Fig. 3-22 shows the process of splicing of Si-cored fiber and single-mode fiber. The fusion splicing loss of Si-cored fibers and Si fibers were shown in Table 3-2.

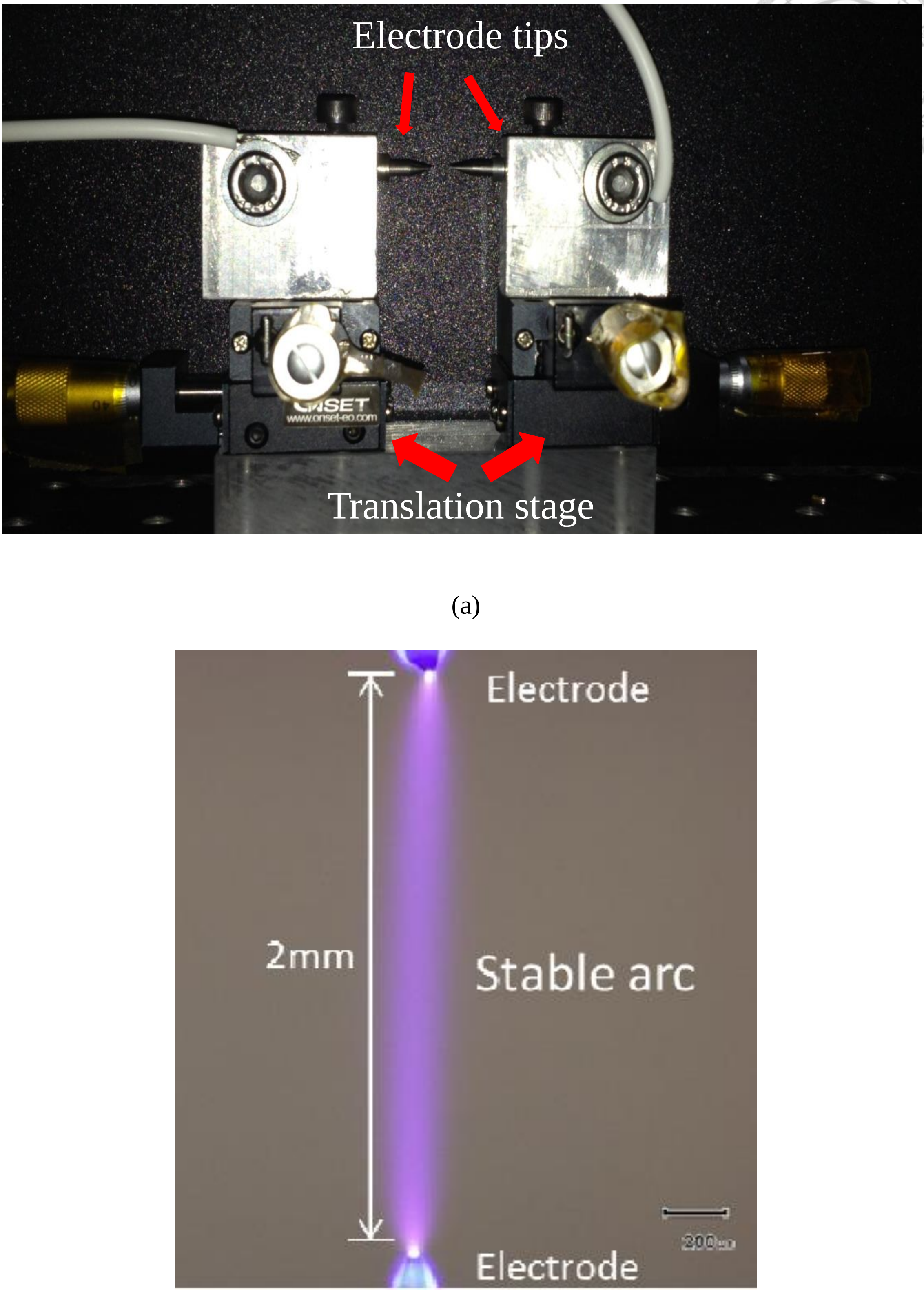

(a)

(b)

Fig. 3-18 (a) Setup of electrode tips devices (b) A stable arc discharge.

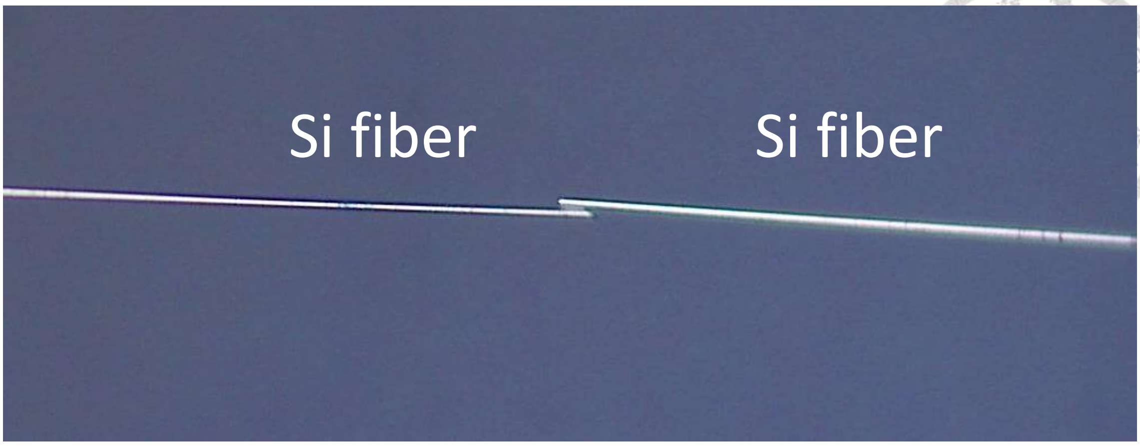

(a)

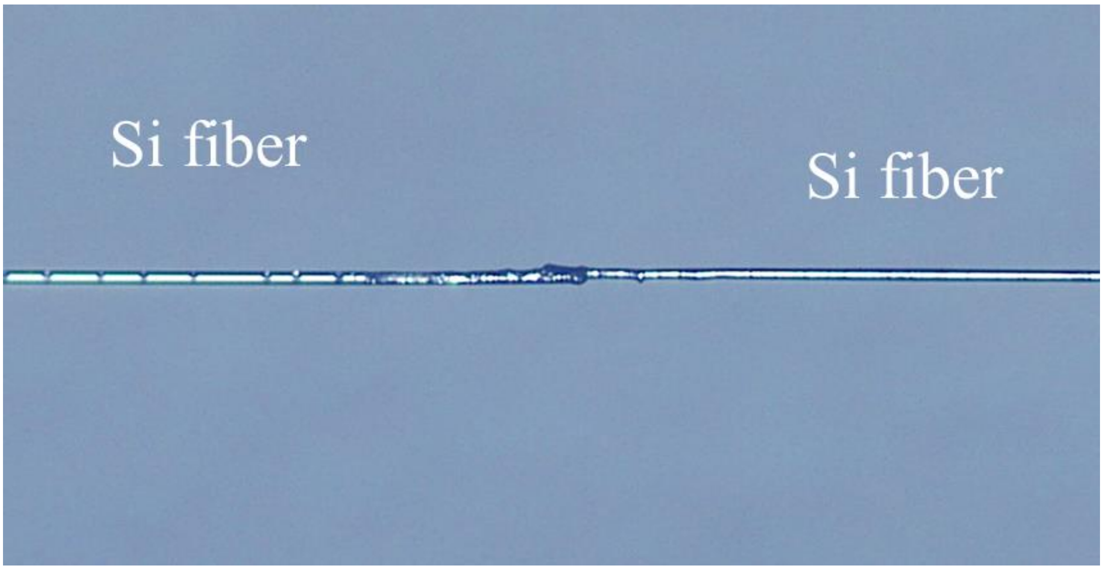

(b)

Fig. 3-19 (a) The optical microscope image of two Si microfibers which were overlapped each other (b) Two Si microfibers melted to become one after arc discharging.

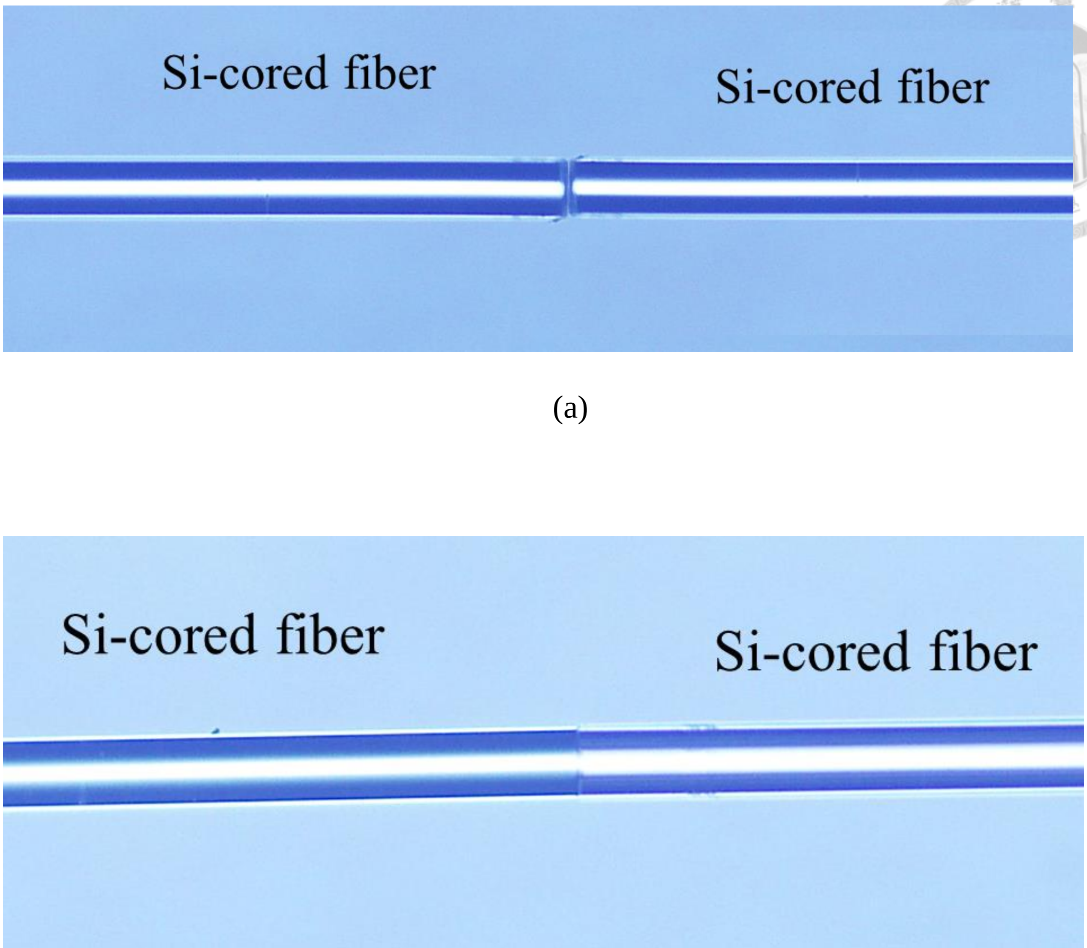

(a)

(b)

Fig. 3-20 (a) The two Si-cored fibers were connected straight to each other (b) A spliced Si-cored fiber after arc discharge.

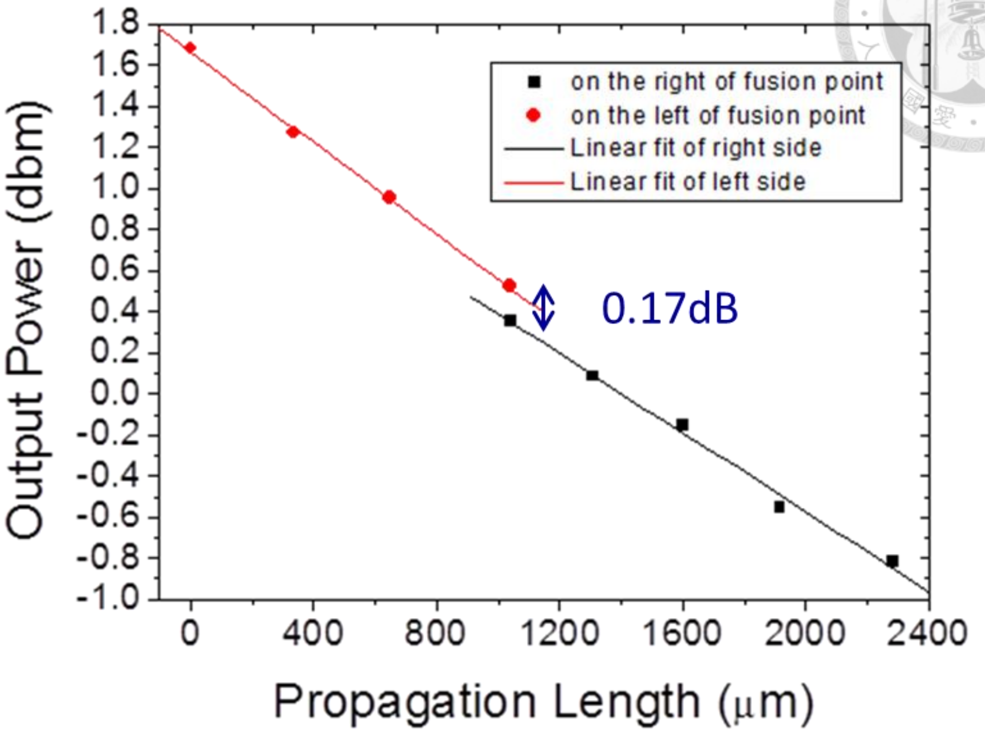

Fig. 3-21 The measured splicing loss of Si microfiber by side coupling method.

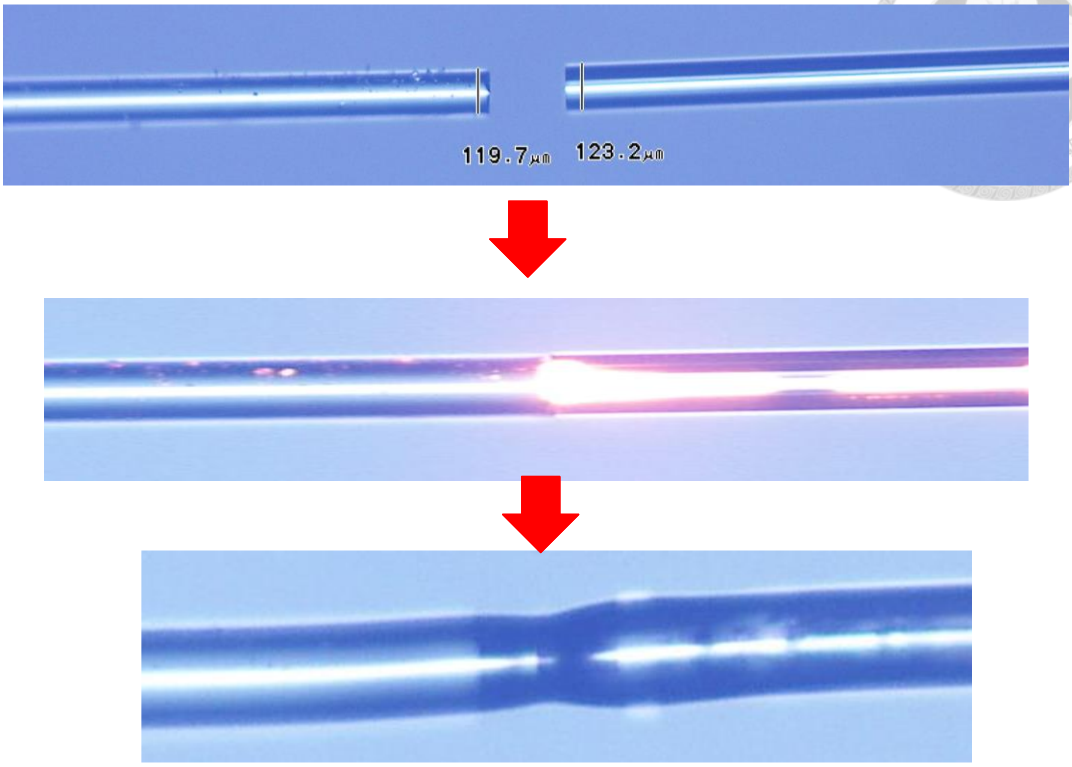

Fig. 3-22 The process of splicing of Si-cored fiber and single-mode fiber.

Arc fusion splicing loss	Si microfiber	Si-cored fiber	Single mode fiber
Si microfiber	0.17dB		
Si-cored fiber		0.47dB	0.7dB

Table 3-2 The splicing loss of different kinds of fibers.

Chapter 4 Schottky Photodetector made on Si-cored fiber

4.1 Motivation

Silicon photonics has recently become a subject of intense interest because it offers opportunities for low cost and low power consumption for applications ranging from telecommunication down to chip-to-chip interconnects [13]. However, a hard issue for silicon photonics is the fabrication of active devices such as light sources and PDs. Because silicon is not a direct bandgap material which cause its inefficiencies in light emission, a silicon light source is often incorporated using a hybrid material based approach. In addition, the near-infrared transparency window limits the usefulness of silicon as an active absorbing material for photodetection. Because the energy of infrared photons is too low to overcome the potential barrier of silicon bandgap (~1.1 eV), few free carriers could be generated. For realization of a monolithic integrated optoelectronic circuits on silicon photonics platform for long-haul communication, different approaches were proposed and demonstrated for light detection including two-photon absorption (TPA) [14, 15], incorporation of optical dopants or defects with mid-bandgap energy levels into Si lattice [16], merging germanium active layer with the silicon-based devices [17-18]. Using TPA could potentially contribute low noise to pure silicon photodetection; however, this approach requires high optical power or realization of high quality factor optical cavity to achieve enhanced photon density. On the other hand, in the cases of germanium integration and introduction of mid-bandgap states into silicon lattice, the main challenge remains to be the reduction of the dark current owing to the lattice mismatch and the presence of defects. An alternative way of detecting infrared sub-bandgap optical radiation in silicon is based on the internal photoemission process [19] to make a Schottky barrier PD [20, 21]. An SSPD consists of two electrodes, ohmic and Schottky contacts, built on a silicon waveguide which is generally fabricated by using reactive-ion etching [22], local-oxidation of silicon [23], etc. Schottky PDs are very attractive because of their well established material structures and fabrication process. However, the silicon waveguide based detectors require complicated semiconductor fabrication process to define their waveguide regions. Besides, the light coupling to such waveguide PDs is practically a tough issue because their inherent small waveguide regions cause large mode mismatches when connected with conventional silica optical fibers. In this work we demonstrate a way to fabricate an SSPD built directly on a silicon cored (Si-cored) fiber. The need of conventional optical fiber aerial coupling can be eliminated because of the feasibility of splicing a Si-cored fiber with a silica optical fiber.

4.2 The Theory of Schottky Junction

A Schottky junction is formed by bringing a metal and a semiconductor into contact. The basic phenomena which lead to the formation of a Schottky junction with an n-type semiconductor are summarized in Fig. 4-1 where E_V is the energy of valence band, and E_C is the energy of conduction band. In thermal equilibrium, when the Fermi levels E_F of the metal and the semiconductor are equalized, a transfer of electronic charge occurs from the semiconductor to the metal in the case where the work function $q \cdot \phi_m$ of the metal and $q \cdot \phi_s$ of the semiconductor(q being the elementary charge; ϕ_m being the electric potential of metal, and ϕ_s being the electric potential of semiconductor, electric potential at a point of space is the amount of electric potential energy that a unitary point charge would have when located at that point.) is greater than the electron affinity χ (the electron affinity is defined as the amount of energy required to detach an electron from a singly charged negative ion.) of the semiconductor, and a space charge region (SCR) appears at the edge of the semiconductor of width Xd next to the junction, where the only charges present are the positively-ionized donors. A curvature of the energy bands therefore occurs at the junction, which leads to the appearance of an energy barrier from metal to semiconductor, called a Schottky barrier, whose height is given to first approximation by the expression in Eq. 4-1 and a energy barrier height from semiconductor to metal is $q \cdot V_{bi}$ which is shown in Eq. 4-2.

$$q \cdot \phi_{Bn} = q \cdot (\phi_m - \chi) \tag{4-1}$$

$$q \cdot V_{bi} = q \cdot (\phi_m - \phi_s) \tag{4-2}$$

In equilibrium, therefore, we find an intrinsic electric field immediately next to the metal-semiconductor junction which is comparable in form to that found in a p-n junction. Consequently, it is the phenomenon of photogenerated charge carriers inside and near to the SCR which is responsible for the appearance of a photocurrent, with the electron-hole pairs being separated by the effect of the electric field in the Schottky junction. It is possible, as in the case of the p-n junction, to modify the intensity of the internal electric field in the junction by applying a bias voltage V between the semiconductor and the metal of the Schottky contact as shown in Fig. 4-1 (c). In the case of an n-type semiconductor, the application of a negative voltage between the semiconductor and the metal electrode of the Schottky contact has the effect of reverse-biasing the Schottky junction, which leads to an increase in the height of the effective barrier along with an increase in the width of the SCR. This last effect is of course favorable for photodetection. Indeed, it follows that the majority charge carriers (electrons) cannot flow towards the Schottky contact, and only the minority carriers (holes) generated by external excitation (in particular photogeneration) can reach the Schottky contact and hence produce an electric current: as in the case of the p-n junction, we therefore find that the current flows in reverse through the Schottky junction, that is, from the semiconductor towards the Schottky contact as shown in Fig. 4-2 The illumination of Schottky photodiodes can occur through the metal or semiconductor face. In the case of illumination through the metal face, we resort to a semi-transparent Schottky contact, characterized by a very small thickness of metal selected to ensure sufficient optical transmission The gain of Schottky photodiodes is at most 1, which would be the case if all the photogenerated charge carriers were collected by the electrodes at the ends of the device. However, the near-infrared wavelength is useless for some indirect band-gap semiconductor such like silicon so the photodetection will be resorted to photoexcitation from the metal as shown in Fig. 4-3.

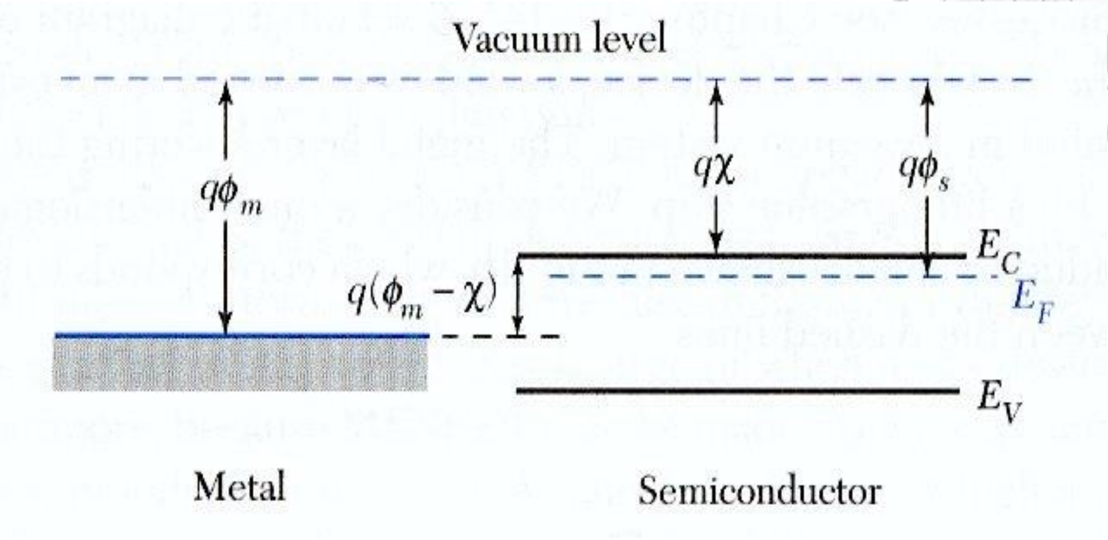
Vacuum level
$q\phi_m$
$q\chi$
$q\phi_s$
E_C
E_F
$q(\phi_m - \chi)$
E_V
Metal
Semiconductor

(a)

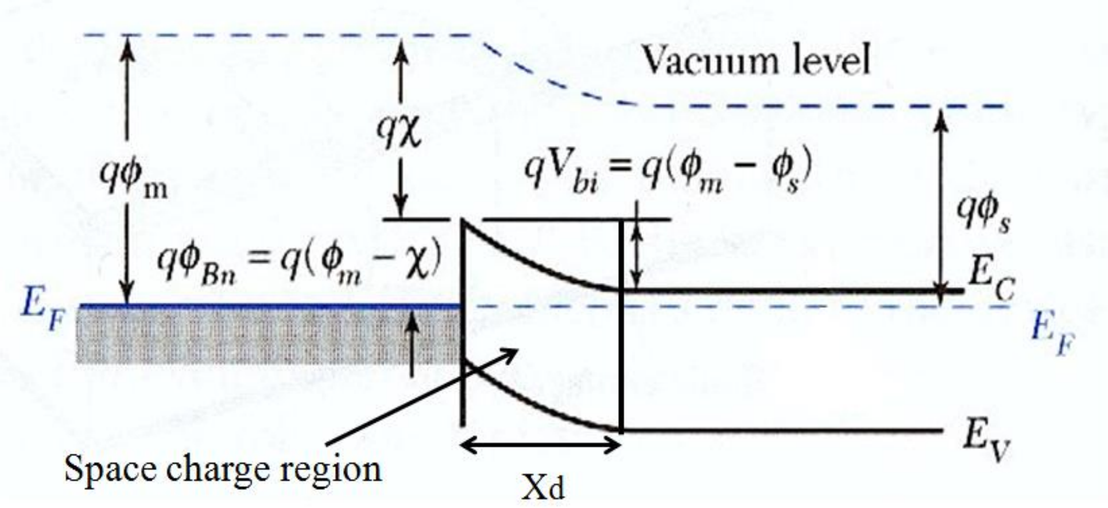
Vacuum level
$q\chi$
$q\phi_{\mathrm{m}}$
$qV_{bi} = q(\phi_m - \phi_s)$
$q\phi_s$
$q\phi_{Bn} = q(\phi_m - \chi)$
E_F
E_C
E_F
E_V
Space charge region
Xd

(b)

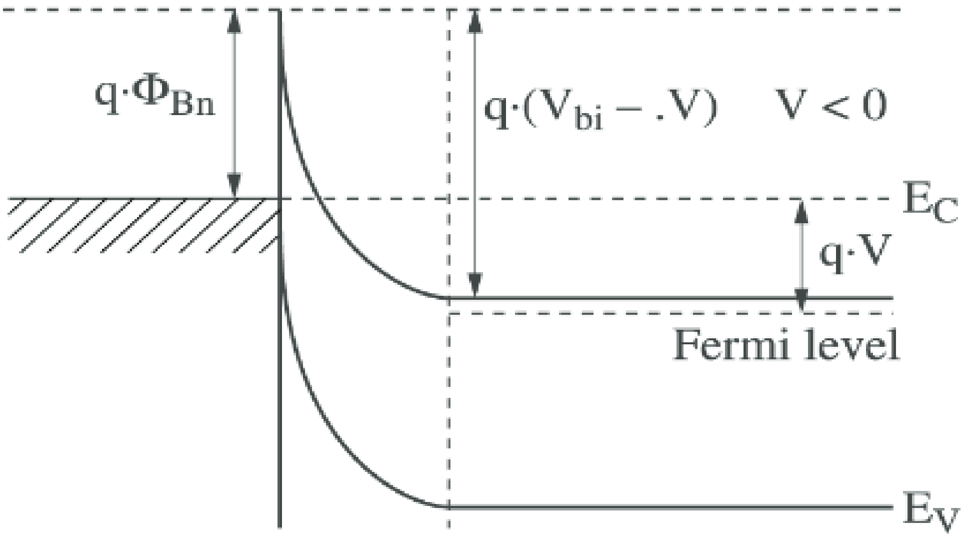

(c)

Fig. 4-1 The energy diagram of metal and n-type semiconductor (a) before contact (b) after contact (c) the energy diagram of Schottky junction under reverse bias V. [24]

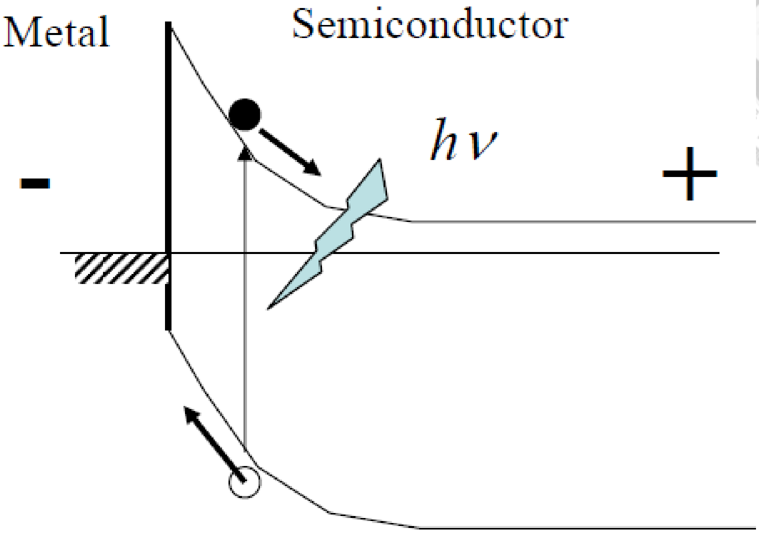

Fig. 4-2 Photoexcitation in the n-type semiconductor under reverse bias. [24]

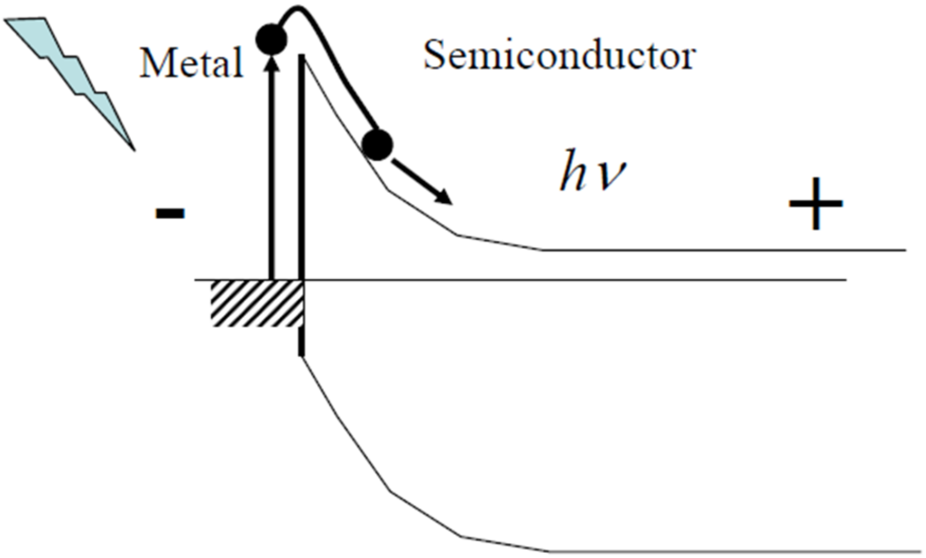

Fig. 4-3 Photoexcitation in the metal by near-infrared wavelength regimes. [24]

4.3 Fabrication of Schottky photodetector on a Si-cored fiber

A Si-cored fiber was placed on a glass substrate and coated with SU8-2100 photoresist which served as etching mask to define the detection and contact areas for metal deposition. Fig. 4-4 shows the schematic fabrication process of defining the detection and contact areas. To expose a circular Si waveguide, the defined silica cladding area of the Si-cored fiber were removed by using buffered hydrofluoric acid solution. To make a Schottky PD, a silver pad as ohmic contact was made first on the silicon fiber, and then a 65 nm thick Au layer was deposited on the fiber and followed by a lift-off process to form the Schottky contact. This PD was fiber ready to be connected with the receiving end of a transmission silica fiber. The splicing of Si-cored fiber was carried out by using an electric arc discharge device, which was already discussed in chapter 3.4. Fig. 4-5 shows the schematic diagram of a Schottky photodector directly made on a Si-cored fiber.

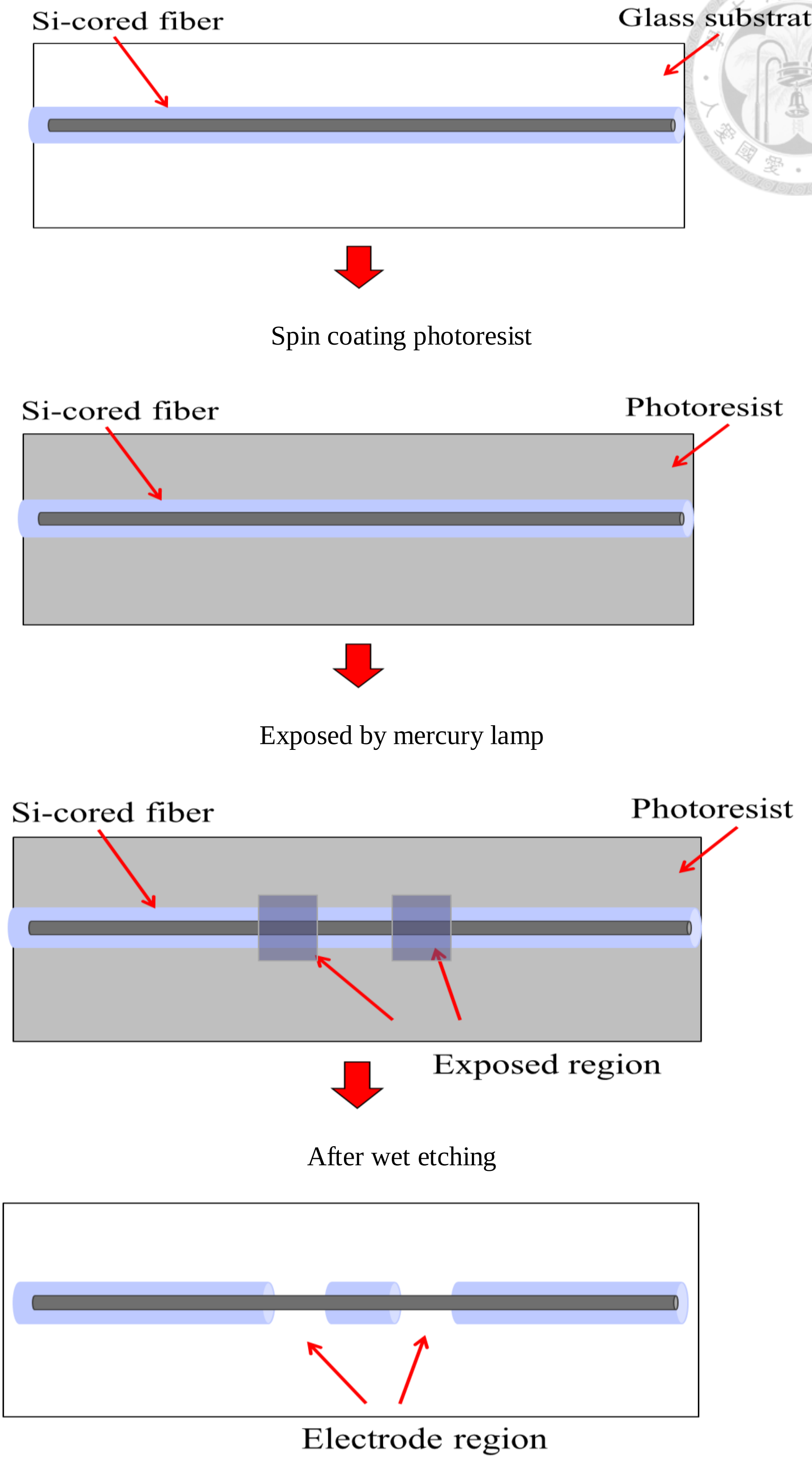
Si-cored fiber
Glass substrate
Spin coating photoresist
Si-cored fiber
Photoresist
Exposed by mercury lamp
Si-cored fiber
Photoresist
Exposed region
After wet etching
Electrode region

(a)

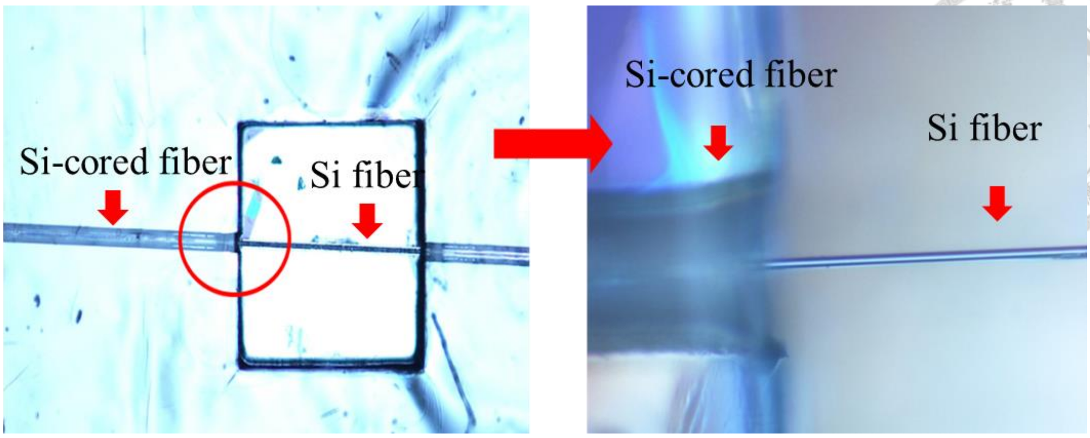

(b)

Fig. 4-4 (a) The schematic fabrication process of defining the detection and contact areas (b) The optical microscope image of the revealed area of Si-cored fiber.

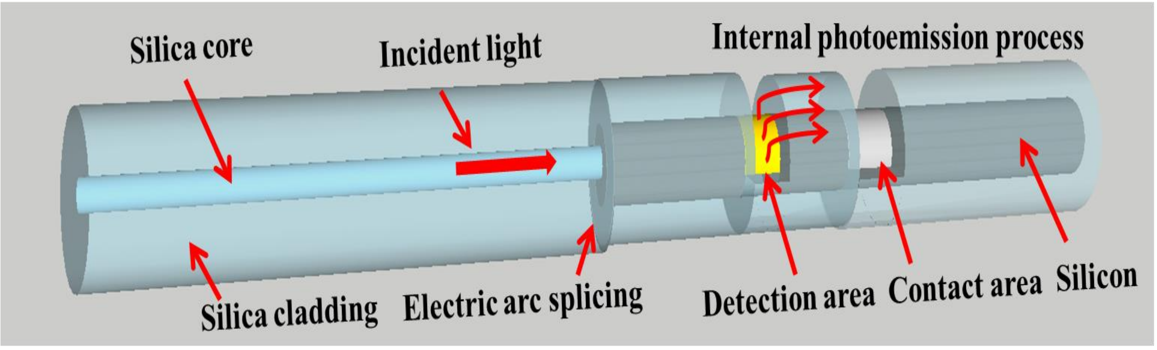

Fig. 4-5 A schematic diagram showing a Schottky photodector directly made on a silicon cored fiber.

4.4 Electrical Characteristics of Schottky Photodetector on Si-cored Fiber

For device characterization, the current-voltage (I-V) characteristics of the SSPD were measured for different optical input power of light operating in 1550 nm wavelength regimes. The measure setup is shown in Fig. 4-6. We used two probe stages to probe the I-V characteristics of SSPD and a tunable laser (LUNA PHOENIX1400) as light source. The probe measurement was monitored by using a CCD to ensure that the probe was properly contact with electrodes. Fig. 4-7(a) shows the measured photocurrent versus reverse bias at different incident optical power. It is clearly seen that the photo-generated carriers increased with bias voltage and light intensity, proving the function as PD. For example, at 0.45V reverse bias, the dark current was found 0.3 μA, and the photocurrent was 1.3 μA for 6.5 mW incident power. A significant figure of merit for a PD is its dynamic range that describes the power range a PD can distinguish. According to Eq. (4-3) [24]

$$I_{dark} = C_{area} A^{**} T^{2} e^{-q\Phi_B / KT} \tag{4-3}$$

where k is Boltzmann's constant; q the electron charge; Φ_B the Schottky barrier; T the absolute temperature; A^{**} the effective Richardson constant (32 and 112 $\mathrm{Acm^{-2}K^{-2}}$ for holes and electrons, respectively [25])); C_{area} the Schottky contact area. The value of Schottky barrier, Φ_B, obtained from our measurement was estimated to be 0.736V, similar to the reported value, 0.744, for n-type silicon-Au Schottky contact [26]. The difference in values may be due to the surface roughness of silicon [27].

The responsivity of the PD was determined by measuring the current across the Schottky contact under reverse bias as a function of the incident optical power. Fig.

4-7(b) shows the measurement result. As expected, the photocurrent increased almost linearly with the input power. The slope of linear fit corresponds to the external responsivity of PD according to $I = I_{dark} + RP_{in}$, where I_{dark} is the leakage current of the detector, P_{in} is the incident optical power and R is the responsivity of the device. Therefore, the responsivity of PD was found 0.226 mA/W at 1550 nm when reverse biased at 0.45 V. Fig. 4-8(a) shows the results of photodetection measurements for increasing incident optical power at different wavelengths without bias. Such results of spectral responses indicate an increased responsivity for shorter wavelengths, which is consistent with the enhanced quantum efficiency of the internal photoemission process for energetic incident photons according to the modified Fowler equation expressed in Eq. 4-4 [28].

$$\eta = C \frac{(h\nu - \Phi_B)}{h\nu} \tag{4-4}$$

where η is the quantum efficiency of photoemission process (number of carriers that contribute to the photocurrent per incident photon), Φ_B is the Schottky barrier, and C is the photoemission coefficient. The quadratic dependence follows from the emission probability being proportional to the density of metal electrons capable of passing the barrier. Finally, by using the responsivity values for different wavelengths with corresponding photon energies, the Fowler plot is obtained as shown in Fig. 4-8(b), which verifies that the measurement results do follow the linear dependence of $R^{1/2}h\nu \propto (h\nu - \Phi_B)$，we could use y axial interception of Fowler plot to estimate the Fowler theorem of Schottky barrier height. The result of theoretical calculation was 0.737 eV which was similar to the result of experiment.

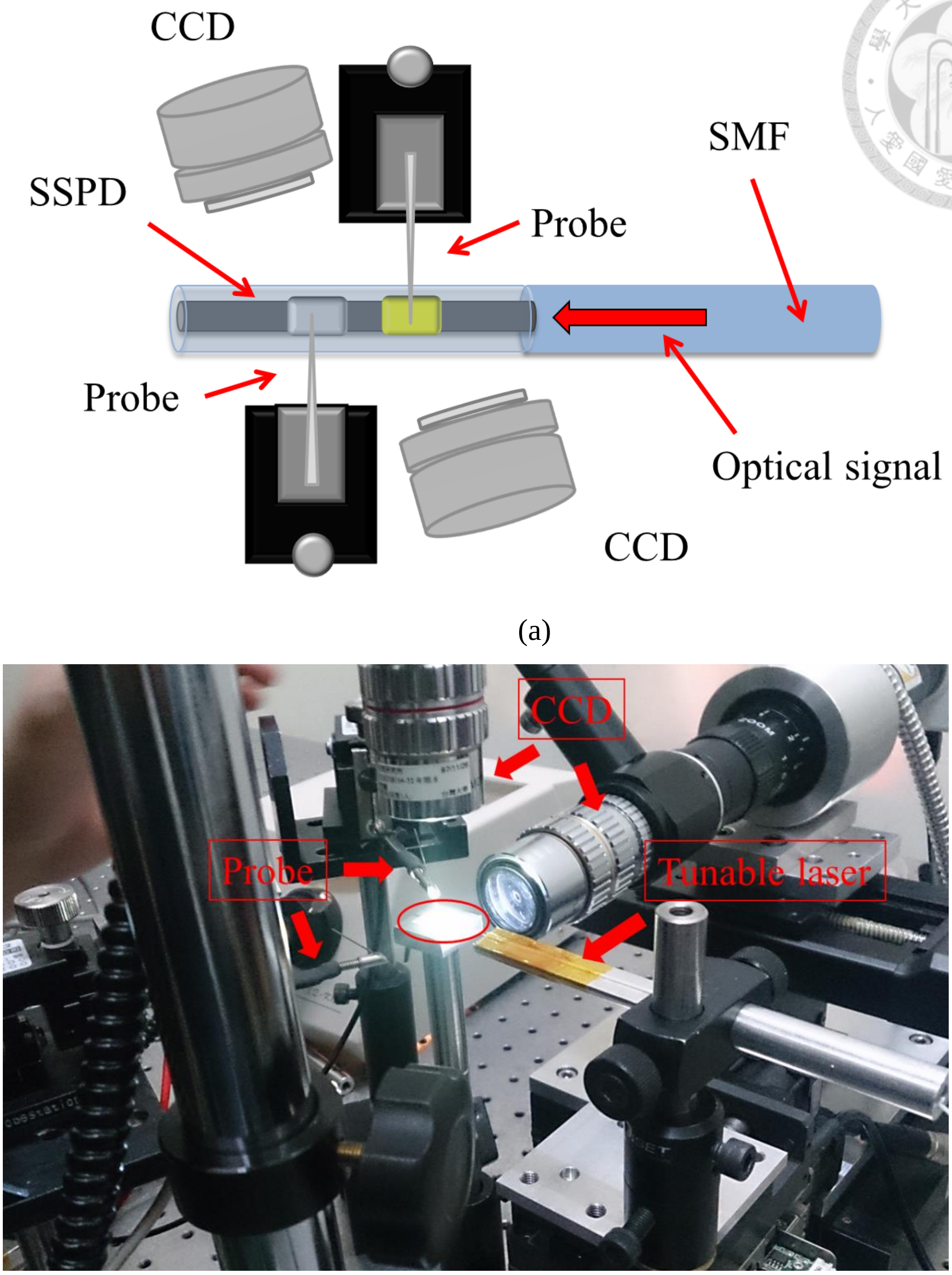

(a)

(b)

Fig. 4-6 (a) A schematic setup for for measuring the I-V characteristics of the SSPD (b) photograph of the I-V characteristics measurement setup.

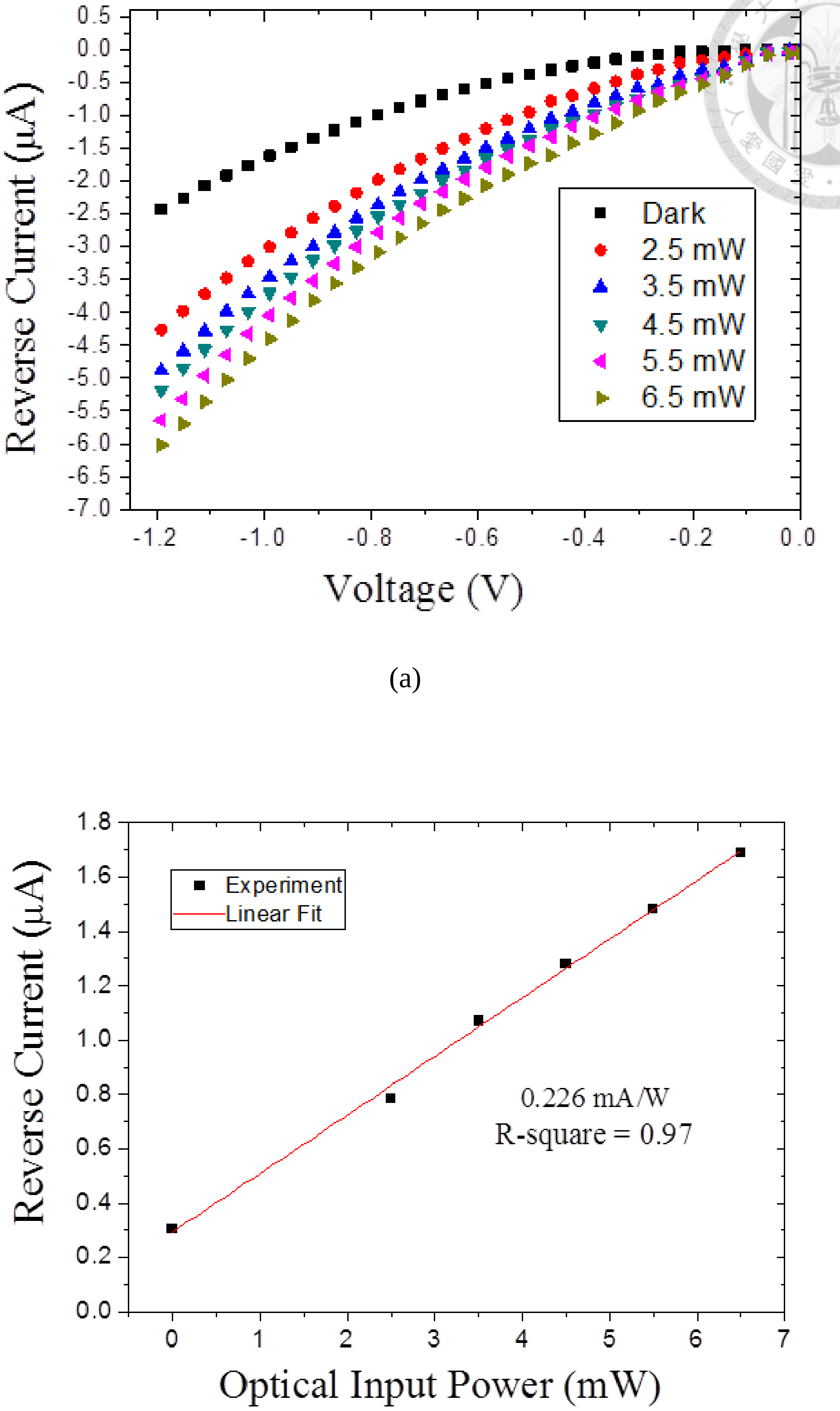

(a)

(b)

Fig. 4-7 (a) Measured photocurrent versus reverse bias for varied optical power. (b) Measured photocurrent versus varied optical power from a 1550 nm laser.

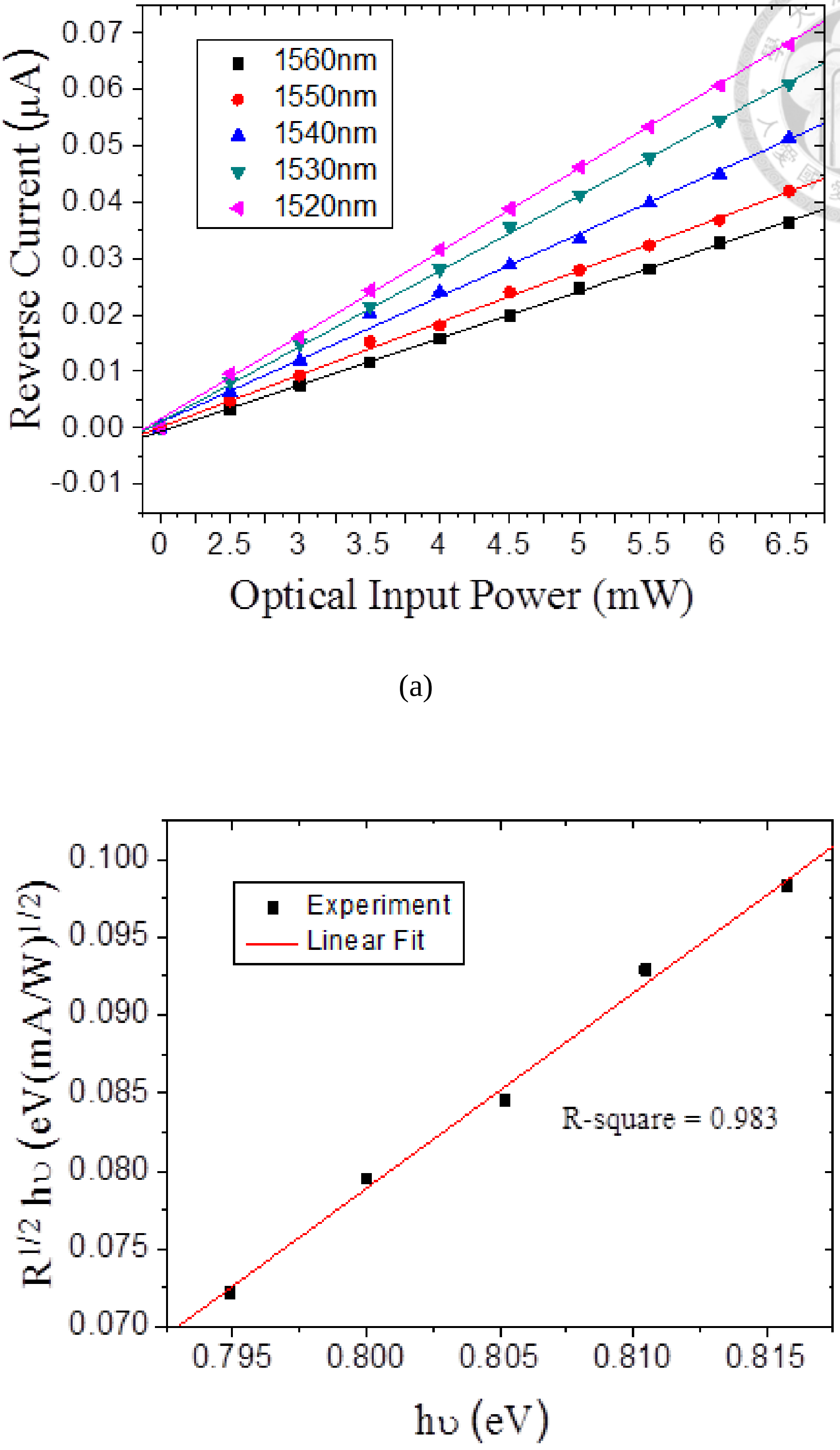

(a)

(b)

Fig. 4-8 (a) Measured photocurrent as a function of incident optical power at wavelengths from 1520 nm to 1560 nm without bias. (b) Fowler plot.

4.5 Bandwidth of Schottky Photodetector

The response time of Schottky barrier photodiodes can be determined by three parameters: the diffusion time in the quasi neutral region; the electrical frequency response or RC time required to discharge the junction capacitance through the resistance and the transit time across the depletion region. In the range of bias voltage (0.5-1 V), the diffusion time can be neglected. For the RC constant limited case, the 3 dB roll-off frequency is shown in Eq. 4-5.

$$f_{RC} = \frac{1}{2\pi R_L C_d} \quad \text{and} \quad C_d = \frac{\varepsilon_{Si} A_{Ph}}{W} \tag{4-5}$$

where A_{Ph} is the area of the photodetector; *W* is the depletion layer width; *RL* is the load resistance; *Cd* is the capacitance due to the depletion layer. The intrinsic carrier-transit time which limits 3 dB bandwidth for the device is given by Eq. 4-6.

$$f_{tr} = \frac{0.44}{t_d} = 0.44 \times \frac{V_t}{L} \tag{4-6}$$

where *Vt* is the effective carrier saturation velocity (107 cm s^{-1}) and *L* is the carrier transit distance. The total frequency is given by Eq. 4-7.

$$\frac{1}{f_{tot}} = \frac{1}{f_{tr}} + \frac{1}{f} \tag{4-7}$$

It is worth noting that when the detector area is made sufficiently small, the influence due to the capacitance will be reduced and the effect of the transit time dominates. Fig. 4-9 shows the schematic diagram of the setup used to measure the frequency response of Schottky PD. Electrical signals from a network analyzer was used to modulate the laser source (E2550 EML Modules) which is designed for Time-division multiplexing transmission applications, and then the optical modulation signals would output to the

Schottky PD which was under reverse bias. The bias could be imposed through a bias tee which is a three port network used for setting the DC bias point of some electronic components without disturbing other components. The low frequency port is used to set the bias; the high frequency port passes the radio frequency signals but blocks the biasing levels; the combined port connects to the device, which sees both the bias and RF. The photocurrent would be delivered to network analyzer through a high frequency cable to measure the response frequency of Schottky PD. We measured the bandwidth of laser source in advance in order to ensure the bandwidth of laser is higher than PD. Fig. 4-10 shows the results of measurement of frequency response of laser source. The bandwidth of laser source is higher than 1 GHz which is high enough to measure Schottky PD. The irregular signal could cause by the inappropriate quality of cables which consist of flexible copper tube. We measured the frequency response of Schottky PD after checked of the bandwidth of laser source. The result of frequency response measurement is shown in Fig. 4-11. The bandwidth of Schotkky PD was estimated to be 30 MHz which could be improved by decreasing the capacitance of PD. According to Eq. 4-5.

$$C_d = \frac{\varepsilon_{S\,f} A_{\;P}}{W} \tag{4-5}$$

capacitance could be reduced by decreasing the metal contact area and increasing the depletion layer width.

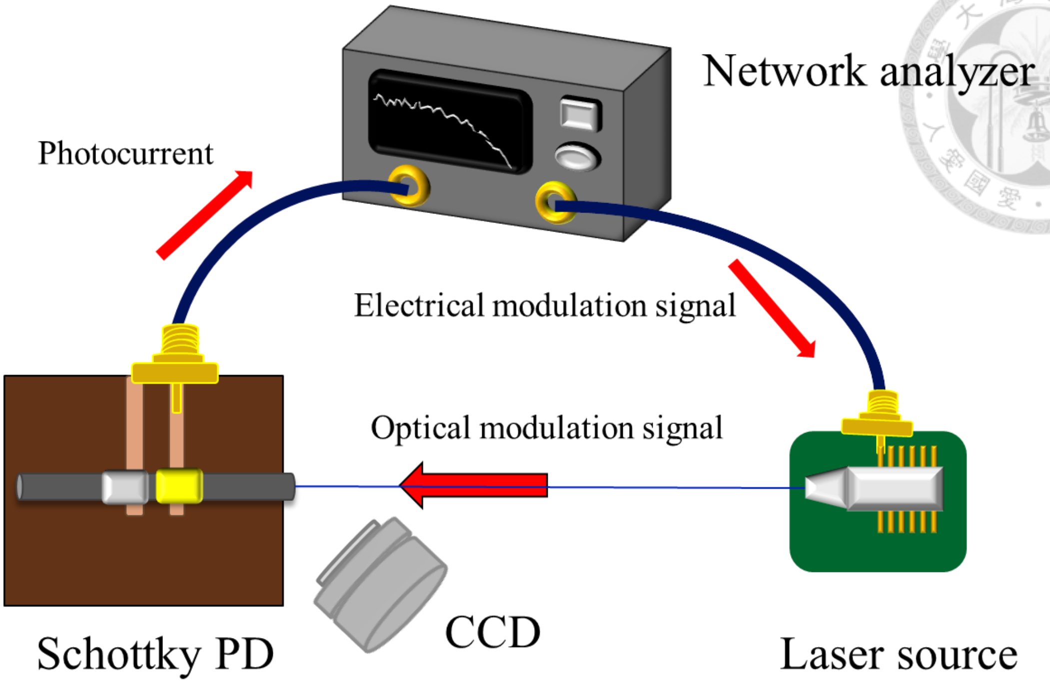

Fig. 4-9 A schematic diagram of the setup of response frequency of Schottky PD.

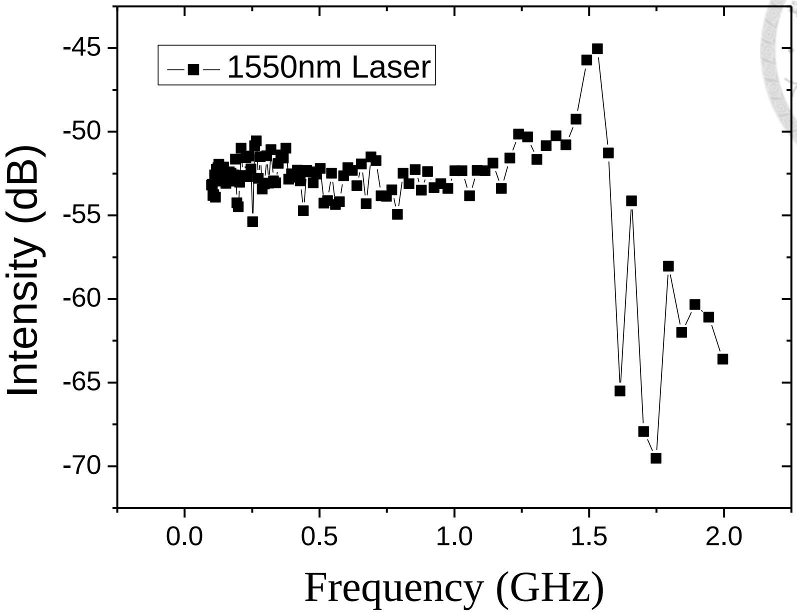

Fig. 4-10 The results of measurement response frequency of laser source.

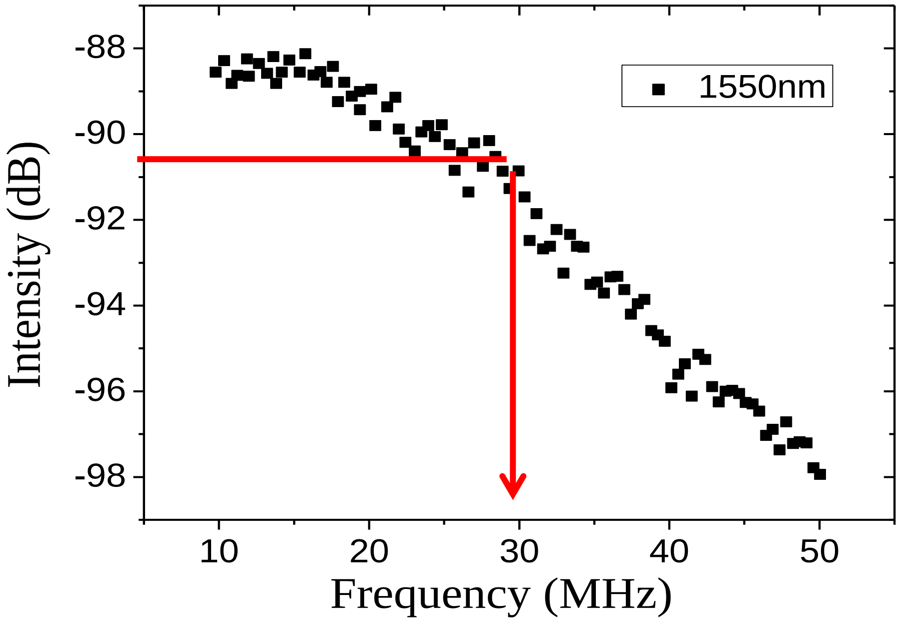

Fig. 4-11 The results of measurement response frequency of Schottky PD.

Chapter 5 Conclusions and Future Works

5.1 Conclusions

Chapters 2 and 3, we demonstrate that superior characteristics can be obtained for single-crystal Si-cored fibers made by using a rapidly vertical drawing method. The use of low-cost polycrystalline Si powders as the preform material paves an economic way of fabricating high quality meter-long single-crystal Si-cored fiber. By optimizing the processing temperature, the soften silica cladding could still provide substantial confinement on the molten Si core during the drawing process. At the higher drawing speed, the rapid and dramatic reduction in the cross-sectional area generates a strong stress and spatial confinement on the Si core, making single crystalline possible. The large stress helps the nucleation of Si crystals and the further high cooling rate keeps the single crystalline phase of Si core after being cooled down to room temperature. The crystallinity transformation from polycrystalline powders into single-crystal phase has been investigated and confirmed by using both the micro-Raman spectroscopy and HR-TEM. According to the HR-TEM images and micro-Raman spectra, the Si core possesses outstanding properties, including single crystallinity, high purity and high uniformity throughout the meters long fiber. In this thesis work, we provide a low-cost, rapid, and large throughput fabrication of single-crystal Si-cored fibers by optimizing the cladding confinement and lateral stress during the drawing process. The ultralow loss single-crystal Si-cored fibers thus fabricated are expected to find applications in the fields of optics and electronics such as photodetectors.

Chapter 4, we demonstrate an SSPD for working in presumably transparent telecom wavelengths by employing the vertical drawing method. This method provides a rapid and simple fabrication process for making a Si waveguide PD without the need of resorting to the conventionally complicated semiconductor process so that it is a potential way to be applied in fabrication of monolithic silicon waveguide based detectors. The dimension of Si cored fibers could be further decreased to facilitate the integration with other devices. Such PDs would be potentially useful for optical fiber applications such as power monitoring and optical interconnects.

5.2 Future Works

To further improve the work of fabrication of Si-cored fiber, an electric spool should be employed in this fabrication process. Once the Si-cored fibers are flexible enough to be coiled around a spool, the speed of the spool can be controlled at constant velocity during the drawing process. Because of the same drawing speed, the uniformity of Si-cored will be better than the previous results.

The future improvement of PD will be on the responsivity and frequency response of PD. Based on the theory of bandwidth of Schottky diodes, the primary work is to decrease the meatal contact area to reduce the parasitic capacitance so the response of PD will be further increased. The higher bandwidth PDs is an essential factor for bringing out the full potential of a receiver because it helps relieve the burden imposed on electrical components and also makes their integration easier.

References

[1] P. J. A. Sazio, A. Amezcua-Correa, C. E. Finlayson, J. R. Hayes, T. J. Scheidemantel, N. F. Baril, B. R. Jackson, D.-J.Won, F. Zhang, E. R. Margine, V. Gopalan, V. H. Crespi, J. V. Badding, *Science* **2006**, *311*, 1583.

[2] J. Ballato and E. Snitzer, Appl. Opt. **1995**, 34, 6848.

[3] J. Ballato, T. Hawkins, P. Foy, R. Stolen, B. Kokuoz, M. Ellison, C. McMillen, J. Reppert, A. M. Rao, M. Daw, S. Sharma, R. Shori, O. Stafsudd, R. R. Rice, D. R. Powers, *Opt. Express* **2008**, *16*, 18675.

[4] B. Scott, K. Wang, G. Pickrell, *IEEE Photonic. Technol. Lett.* **2009**, *21*, 1798.

[5] J. Blyler, L.L and F. V. DiMarcello, Proc. IEEE, **1980**, 68, 1194.

[6] U. Paek, J. Lightwave Technol, **1986** , 4, 1048.

[7] U. C. Paek, J.Heat Transfer, **1999**, 121, 774.

[8] D. J. Won, M. O. Ramirez, H. Kang, V. Gopalan, N. F. Baril, J. Calkins, J. V. Badding, P. J. A. Sazio, *Appl. Phys. Lett.* **2007**, *91*, 161112.

[10]N. Healy, J. R. Sparks, P. J. A. Sazio, J. V. Badding, A. C. Peacock, *Opt. Express* **2010**, *18*, 7596.

[11] Jacoboni, C., C. Canali, G. Ottaviani, and A. A. Quaranta, *Solid State Electron.*, **1977,** 20, 77.

[12] S. Morris, T. Hawkins, P. Foy, J. Hudson, L. Zhu, R. Stolen, R. Rice, and J. Ballato, Optical Materials Express **2012,** 2, 1511.

[13] L. Pavesi and G. Guillot, *Optical Interconnects: The Silicon Approach* , **2000.**

[14] D. W. Peters, Proc. IEEE **1967**, 5, 704.

[15] Tanabe, T.; Sumikura, H.; Taniyama, H.; Shinya, A.; Notomi, M. Appl. Phys. Lett. **2010**, 96, 101103.

[16] Bradley, J. D. B.; Jessop, P. E.; Knights, A. P. Appl. Phys. Lett. **2005**, 86, 241 103

[17] P. Mehta, N. Healy, N. F. Baril, P. J. A. Sazio, J. V. Badding, and A. C. Peacock, Opt. Express **2010,** 18, 16826

[18] Assefa, S.; Xia, F.; Vlasov, Y. A. Nature, **2010**, 464, 80.

[19] Liang, T. K.; Tsang, H. K.; Day, I. E.; Drake, J.; Knights, A. P.; Asghari, M. Appl. Phys. Lett. **2002**, 81, 1323.

[20] S. Zhu, M. B. Yu, G. Q. Lo, and D. L. Kwong, Appl. Phys. Lett. **2008,** 92, 081 103.

[21] M. Casalino, L. Sirleto, M. Iodice, N. Saffioti, M. Gioffre`, I. Rendina, and G. Coppola, Appl. Phys. Lett. **2010,** 96, 241 112.

[22]S. M. Sze, and K. K. Ng, *Physics of Semiconductor Devices*, Wiley, New York, USA, **2006**.

[23] I. Goykhman, B. Desiatov, J. Khurgin, J. Shappir, and U. Levy, Nano Lett. **2011,** 11, 2219.

[24] P. Kramer, and L. J. van Ruyven, Appl. Phys. Lett. **1972**, 20, 420.

[25] Ali Akbari, R. Niall Tait, and Pierre Berini, Opt. Express **2010**, 18, 8505.

[26] Michel, J.; Liu, J.; Kimerling, L. C. High-performance Ge-on-Si photodetectors. Nat. Photonics, **2010**, 4, 527.

[27] M. A. Yeganeh and S. H. Rahmatollahpur, J. Semicond. **2010**, 31, 07400.

[28] Scales, C. and Berini, IEEE J. Quantum Elect. **2010**, 46, 633.